UNIVERSITY OF COPENHAGEN

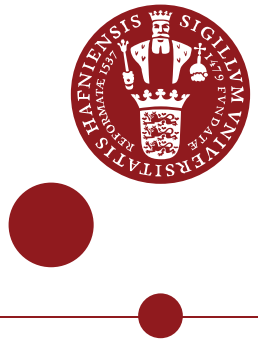

MSc in Physics

Exploring the chemical enrichment of galaxies within 600 Myr after the Big Bang

Isabella Henum

Supervised by Victoria B. Strait, Kasper E. Heintz and Gabriel B. Brammer

22nd of May 2023

Isabella Henum

Exploring the chemical enrichment of galaxies within 600 Myr after the Big Bang

MSc in Physics, 22nd of May 2023

Supervisors: Victoria B. Strait, Kasper E. Heintz and Gabriel B. Brammer

University of Copenhagen

Faculty of Science, Niels Bohr Institute

The Cosmic Dawn Center

Jagtvej 128

2200 Copenhagen N

Abstract

Throughout the last 12 Gyr of cosmic time, galaxies have been observed to follow a universal relation known as the fundamental metallicity relation (FMR), which connects the star formation rates (SFRs), stellar masses and chemical abundances of galaxies. With spectroscopic data from the James Webb Space Telescope (JWST), it is now for the first time possible to reliably measure the chemical abundances of galaxies within the first few Myr after the Big Bang, at redshifts $z > 7$, and investigate whether these galaxies follow the FMR. In this thesis, I will present how I first familiarize with spectroscopy, by collecting the wavelength of each visible emission line in spectroscopic observations obtained with the Multi-Object Spectrometer for Infrared Exploration (MOSFIRE). I then proceed to utilize spectroscopic data obtained with the Near-Infrared Spectrograph (NIRSpec) on the JWST to measure the gas phase oxygen abundance of two high redshift galaxies denoted RXJ_95 and SMACS_85, at redshifts $z = 9.5$ and $z = 8.5$ respectively. I determine the oxygen abundance by employing two methods: one based on the electron temperature of the ionized gas and one using empirical strong line calibrations. For both galaxies, I find that their SFRs are higher than for galaxies with similar masses in the local universe, while their oxygen abundances are lower. Although these results align with observational expectations, I also find that the oxygen abundances of the galaxies are significantly lower than predicted by the FMR, suggesting that this relation is not universal at redshifts $z > 8$. This may imply that high redshift galaxies are closely connected with the intergalactic medium and subject to continuous infall of metal poor gas which effectively dilutes their metal abundances in the interstellar medium.

Acknowledgements

First and foremost, I want to thank my supervisors Victoria Strait and Kasper Heintz for their excellent guidance throughout the process of making this thesis. Thank you for your time, patience, and encouragement. You have welcomed me into your offices and I could always count on you to discuss the questions that I have had. Working with you both has been a truly inspiring experience that has taught me so much.

I want to thank my supervisor Gabriel Brammer for providing me with reduced and calibrated data, that I have utilized throughout this thesis. Also, thank you for giving me valuable feedback and great ideas on how to move forward with my data analysis.

I am also very grateful to Charlotte Mason for making me a part of her research group and weekly meetings, where I have gained extended knowledge on various perspectives on the early universe.

Last but not least, I want to thank my parents, my brothers, my grandmother and my boyfriend. Your support means everything to me.

Contents

List of Figures

List of Tables

1 Introduction

1.1 The Epoch of Reionization

The Epoch of Reionization (EoR) refers to the period in approximately the first billion years of the Universe's history, where the intergalactic medium (IGM) transitioned from a neutral to an ionized state. While the exact starting point of the EoR is still subject to debate, it's generally believed to have begun after redshift $z \sim 20$ (Robertson *et al.*, 2010), corresponding to about 150 million years after the Big Bang. Recent observational evidence suggests that the EoR ended around redshift $z \sim 6$ (Fan *et al.*, 2006, Wang *et al.*, 2020), roughly 1 billion years after the Big Bang.

The formation of the first luminous sources, such as stars and galaxies, led to local ionized regions, powered by their intense ultraviolet radiation. Over time, these sources gradually ionized the neutral hydrogen gas in the IGM. The EoR is determined by how and when the Universe started forming luminous sources and how the ionizing radiation from these permeates and fills the IGM. Figure 1.1 shows a cartoon of the cosmic evolution during the EoR, where most of the gas was neutral at the highest redshifts. As the process of reionization progressed, a patchwork of neutral hydrogen (HI) and ionized hydrogen (HII) regions evolved and expanded, until the ionized regions filled the whole Universe (e.g. Zaroubi, 2012).

Exploring the evolution of the IGM during the EoR provides valuable information about the first galaxies in their early stages, and the physical processes that govern them. By understanding these processes and how they differ from those in the local universe, we can gain insights into the evolution of galaxies and their properties over cosmic time.

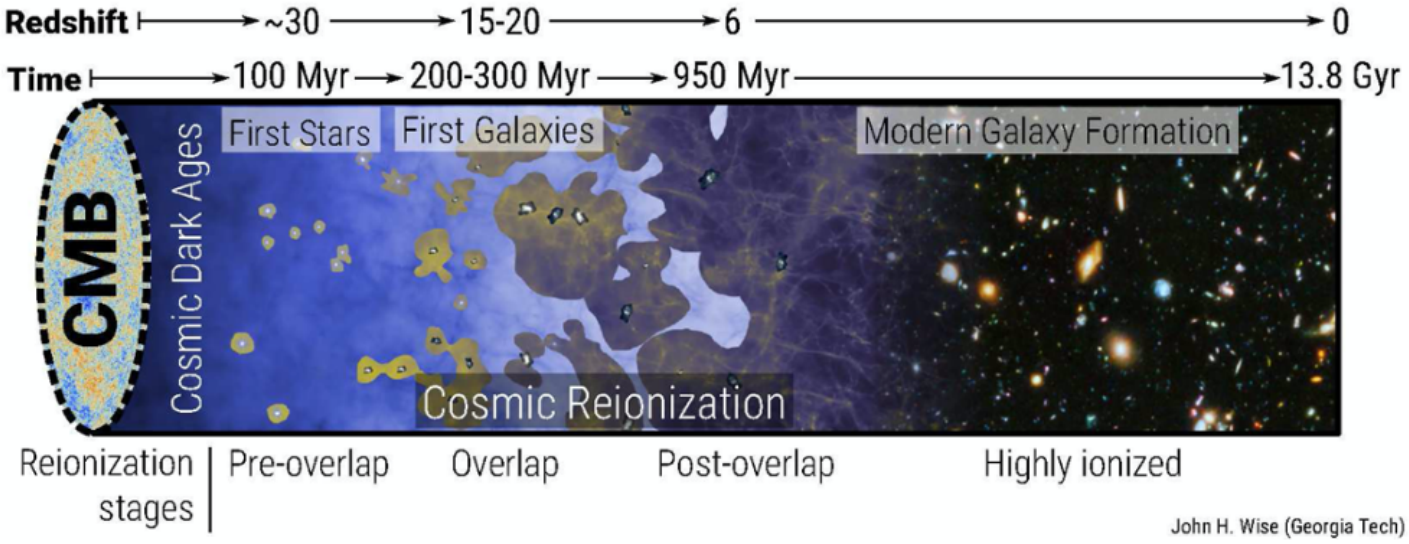

Figure 1.1: The cosmic timeline of the Universe centered around the EoR. The blue colors indicate the neutral regions, while the brown filaments indicate the ionized regions (Wise, 2023).

1.2 From primordial gas to star formation and chemical enrichment

The first galaxies formed during the EoR, when slight fluctuations in the density of matter started to grow larger under the influence of gravity. As matter accumulated, large structures emerged, within which gas and dust collapsed under gravity, eventually reaching a critical threshold allowing the formation of stars. The emergence of the first stars marked the beginning of galaxy formation. Over time, the galaxies underwent a gradual evolution, transforming their structures and properties through various processes such as mergers, interactions with their own and surrounding environment, and continuous formation of new stars from the gas available in the interstellar medium (ISM).

As stars formed and evolved, galaxies gradually became chemically enriched by metals. Metals are defined as all elements other than hydrogen and helium, and are created in stars through nucleosynthesis. This process involves the fusion of hydrogen into helium, which then fuses into heavier elements up to iron (Fe). The metals are released into the ISM through supernovae and stellar winds where they mix with the surrounding gas, enriching it with heavier elements. Once in the ISM, the metal content is shaped by a complex interplay between gas inflow from the IGM and outflow via galactic

winds. The large inflows consists of metal-poor gas and temporarily dilute the metal abundance of the gas in the ISM, but provide the raw materials for star formation over longer periods, ultimately leading to an enrichment of metals.

Studying the gas phase metal abundance of galaxies across cosmic time can provide valuable insights into the mechanisms responsible for the chemical enrichment of galaxies. Mannucci *et al.* (2010) first proposed a scaling relation between the stellar mass, SFR and gas-phase metal abundance of galaxies in the local universe, denoted the fundamental metallicity relation (FMR). The FMR was meant to describe both SFR and metal abundance fluctuations at fixed mass and their redshift evolution where, with increasing lookback time, the SFR per mass goes up and the oxygen abundance goes down, thus keeping galaxies on the FMR. Based on an extensive sample of galaxies Sanders *et al.* (2021) established that the local FMR holds at redshift $z \sim 3$, indicating that galaxies undergo a gradual baryonic growth process in a state of near-equilibrium from redshifts $z \sim 0 - 3$, i.e. from 2 Gyr after the Big Bang to present time. With the James Webb Space Telescope (JWST) it has become possible to investigate whether the FMR holds at higher redshifts. Few studies have already investigated the metal abundances of high redshift galaxies at $z > 7$ (Heintz *et al.*, 2023b, Nakajima *et al.*, 2023, Curti *et al.*, 2023) and find that these galaxies seem to have lower metal abundances than predicted by the FMR. This implies that the FMR is not universally valid at redshift $z > 7$, and that the processes that regulate galaxy evolution, has changed over cosmic time.

1.3 Spectroscopic observations of the early universe

Spectroscopy is a powerful tool, that can be used to study the light emitted by a galaxy, by dispersing it into its component wavelengths. When atoms or ions in a gas are excited by a source of energy, such as heat or radiation by stars, their electrons move to higher energy levels. As they return to lower energy levels, they emit photons of light at specific wavelengths corresponding to the energy difference between the levels involved. These energies appear as bright emission lines in a spectrum, and their position and intensity can be used to identify the presence of chemical elements and their composition in a gas.

As the Universe expands, the distance between us and other galaxies progressively increases over time. Consequently, their emitted light is redshifted, causing a shift of their spectral lines towards longer wavelengths. For example, rest frame optical emission lines emitted by sources at redshifts $z \sim 8 - 10$ will be shifted towards the infrared part of the spectrum. Specifically, their rest-frame wavelength will be shifted by a factor of $(1 + z)$. The redshift of a source (z), the rest-frame wavelength of an emission line (λ_{emit}), and the observed wavelength of an emission line (λ_{obs}) are related via following equation:

$$z = \frac{\lambda_{obs} - \lambda_{emit}}{\lambda_{emit}} \tag{1.1}$$

At high redshifts, emission lines become fainter and more noise arise in the spectra, posing challenges for spectroscopic observations. However, thanks to the JWST, these observations have been significantly improved, enabling more detailed observations of the high redshift universe than ever before. With a primary mirror that measures 6.5 meters in diameter and extremely sensitive near-infrared instruments, JWST is capable of detecting rest-frame optical emission from galaxies at redshifts as high as $z \sim 20$ (Kalirai, 2018), which far surpasses the capabilities of its predecessor, the Hubble Space Telescope (HST). With the JWST, it is possible to gather a large number of high resolution spectroscopic observations of galaxies that formed within the first few Myr after the Big Bang. This provides new opportunities to investigate the chemical enrichment of galaxies at high redshifts $(z > 7)$ and to gain insight into the physical processes that regulate galaxy evolution in the early universe.

1.4 Research questions

The research questions that motivate this thesis are based on trying to understand the chemical enrichment of galaxies at redshifts $z \sim 8 - 10$. Does the FMR hold at high redshifts? Is there different physics driving the chemical enrichment of galaxies in the early universe than in the local universe? How does galaxies' chemical abundances track with other galactic properties at various redshifts? Throughout this study, I work with spectroscopic observations, that I familiarize with by investigating emission lines in observations obtained with the Multi-Object Spectrometer for Infrared Exploration (MOSFIRE). I use spectroscopic observations obtained with JWST to measure the oxygen abundance of two highly magnified low mass galaxies RXJ_95 and SMACS_85

at redshifts $z = 9.5$ and $z = 8.5$ respectively. I compare these results to empirical scaling relations obtained by other studies at various redshift, such as the FMR that has been obtained in the local universe (Mannucci *et al.*, 2010, Curti *et al.*, 2020, Andrews and Martini, 2013), and proven to hold out to a redshift of $z \sim 3$ (Sanders *et al.*, 2021). By analyzing galactic properties and oxygen abundance measurements at high redshifts, I hope to contribute to a more comprehensive understanding of the chemical enrichment of galaxies in the early universe, and how it has changed over cosmic time.

In Chapter 2, I will start by introducing the basic theory on which my thesis is based. I will then move on to present the methods I have used in Chapter 3, to obtain my results. This includes how I got introduced to spectroscopy by working with data from the MOSFIRE archive in Chapter 3.1, and my spectroscopic analysis, calculations, and description of properties, including the oxygen abundances of two high redshift galaxies observed with JWST, in Chapter 3.2. In Chapter 4, I will present and analyze the oxygen abundance measurements and compare them to empirical scaling relations from other studies. I will continue to discuss the results in Chapter 5, together with some future perspectives. Finally, I will conclude my work in Chapter 6.

2 Theory

In this chapter, I will introduce the basic theory on which my thesis is based. I will explain how the oxygen abundance is expressed in Chapter 2.1, and how it is determined in Chapter 2.2. In Chapter 2.3 I will describe the empirical scaling relations that I will utilize to analyse and discuss my results.

2.1 Defining the oxygen abundance

Metals refers to all elements heavier than helium. The relative abundance of two generic elements X and Y is generally expressed in terms of relative number densities (N), comparative to the Solar value, with the notation:

$$[X/Y] = log(N_X/N_Y) - log(N_X/N_Y)_\odot \tag{2.1}$$

The abundance of metals is often measured relative to the abundance of hydrogen, which is the most abundant element in the Universe. When expressing the abundance of chemical elements relative to hydrogen, Equation 2.2 is often used, where the value 12 is introduced. The least abundant elements in the Sun, such as uranium, rhenium, and thorium have abundances of the order of one per 10^{12} hydrogen atoms, so adding 12 makes sure that any element, even the most rare, has positive solar abundance values.

$$12 + log(X/H) = 12 + log(N_X/N_H) \tag{2.2}$$

The metal abundance is often defined and expressed in terms of the oxygen abundance, as this is one of the most abundant metals in the Universe. The terms 'metallicity' and 'oxygen abundance' are often used interchangeably, but they are two different definitions, with the metallicity being the abundance ratio with respect to the solar

value. Throughout this thesis I will measure and refer to the oxygen abundance, given by:

$$12 + log(O/H) = 12 + log(N_O/N_H) \tag{2.3}$$

Oxygen has many strong emission lines, making it relatively easy to measure its abundance in high redshift galaxies using spectroscopic techniques (Maiolino and Mannucci, 2019). The solar oxygen abundance, which serves as a reference value, is given by $12 + log(O/H)_\odot = 8.69 \pm 0.05$ (Asplund *et al.*, 2009).

2.2 Measuring the gas phase oxygen abundance in galaxies

Spectroscopic analysis and the study of emission lines from different ions and atoms in a galaxy can be used to determine the gas phase oxygen abundance in various ways. I will focus on two in this thesis: a method that directly measures the oxygen abundance from the electron temperature, and a method that utilizes strong line calibrations that have been empirically obtained.

2.2.1 The direct T_e method

The oxygen abundance of the ionized gas in the ISM of a galaxy can be measured directly from the temperature of the electrons - this method I will refer to as the direct T_e method.

A few ions, of which doubly ionized oxygen (OIII) is a good example, have energy level structures that result in emission lines from two different upper levels, with considerably different excitation energies occurring in the optical wavelength region. The energy levels of the OIII ion are shown in Figure 2.1, where it can be seen that the [OIII]λ4363 line (also referred to as the auroral line), comes from the upper ^{1}S level, while the [OIII]λ4959 and [OIII]λ5007 lines come from the intermediate ^{1}D level. The relative rates of excitation to the ^{1}S and ^{1}D level depend strongly on the electron temperature.

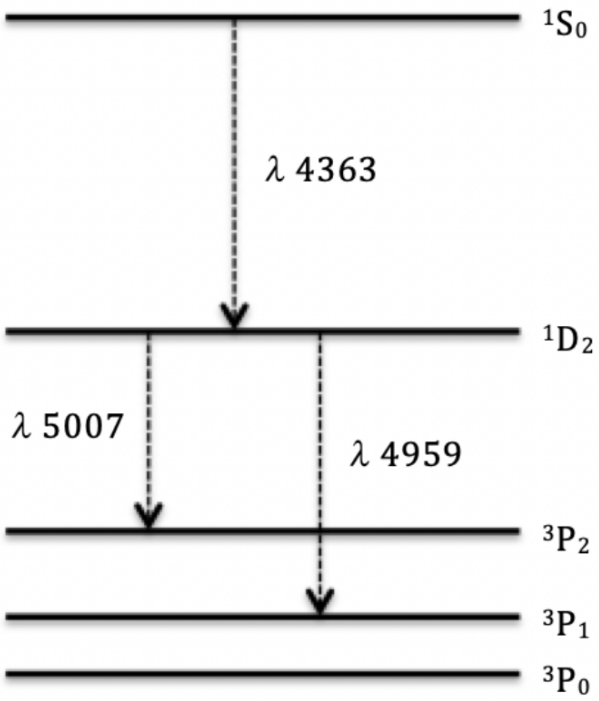

Figure 2.1: Energy level diagram for the lowest terms of the OIII ion, showing transitions that make the determination of the electron temperature possible (Osterbrock and Ferland, 2006).

At low electron temperatures, the higher energy level ^{1}S of the OIII ions are not significantly populated, so the intensity of the [OIII]λ4363 line is weaker. At higher electron temperatures however, these levels become more populated, leading to a higher intensity of the [OIII]λ4363 line relative to the [OIII]λ4959 and [OIII]λ5007 lines. Meanwhile, the relative intensities of the [OIII]λ4959 and [OIII]λ5007 lines remain more or less constant over a wide range of electron temperatures, because they arise from transitions between intermediate energy levels that are not as sensitive to changes in temperature.

At low densities, the population of the various levels will depend on their relative transition probabilities. Every excitation to the ^{1}D level results in emission of a photon either in [OIII]λ5007 or [OIII]λ4959, with relative probabilities given by the transition probability close to 3 to 1. Every excitation to the ^{1}S level is followed by emission of a photon in either [OIII]λ4363 or [OIII]λ2321 (not indicated in Figure 2.1), again with relative probabilities given by the transition probabilities. Each emission of a [OIII]λ4363 photon further results in the population of the ^{1}D level, which again is followed by emission, but this contribution is small compared to the direct excitation of the ^1D level and can be neglected. The ratio of the emission line strengths in the low density limit thereby depends on a combination of the levels collision strengths,

transition probabilities, transition frequencies and the Boltzmann distribution, which depend on the energy difference between the ^{1}D and ^{1}S levels and the temperature. The excited levels are assumed to be populated according to the Boltzmann distribution, meaning that gas particles are assumed to be in local thermal equilibrium (LTE).

At electron densities $N_e \sim 10^5$ cm^{-3}, collisional deexcitation begins to play a role. The lower ^{1}D level has a much longer radiative lifetime than the ^{1}S level, so it is collisionally deexcited at lower electron densities than the ^{1}S level, which causes a weakening in [OIII]λ4959 and [OIII]λ5007. In addition under these conditions, collisional excitation to the ^{1}S level from the excited ^{1}D level begins to strengthen [OIII]λ4363. Generally in the ionized regions of galaxies, the electron density is expected to be $N_e < 10^5$ cm^{-3} (Osterbrock and Ferland, 2006).

The oxygen abundance can be obtained by comparing the flux of the collisionally excited oxygen emission lines to the flux of the hydrogen emission lines. Unlike for the metals, hydrogen's emission lines primarily arise due to a cascade of transitions that occur after the recombination of a proton and a free electron. The electron can occupy a range of excited states, and produces the characteristic hydrogen emission lines that are observed in ionized gas regions. By measuring the flux ratio between the collisionally excited oxygen emission lines and the hydrogen lines arising due to recombination, as well as the electron temperature, the ionic abundance of an element can be derived directly from atomic physics.

The direct T_e method is considered as one of the most precise methods to measure the gas phase oxygen abundance, as it measures the oxygen abundance directly from a galaxy's spectra. However, the method is associated with a few assumptions, one of which is the assumption of LTE, which may not always hold true due to fluctuations in thermal and density structures of the galaxies.

2.2.2 The strong line calibration method

To apply the direct T_e method, a high resolution spectra is necessary, so that all the emission lines required to determine the electron temperature is present. At high redshifts the auroral line needed to apply the direct T_e method are generally very weak, and have only been detected in a handful of sources. This issue has prompted astronomers to obtain empirical calibrations that connects the oxygen abundance to strong emission lines, which can be detected more easily, even in low signal to noise

spectra. This technique is often referred to as the strong line calibration method, and has been obtained in numerous different studies (Curti *et al.*, 2017, Curti *et al.*, 2020, Maiolino *et al.*, 2008, Bian *et al.*, 2018, Nakajima *et al.*, 2022, Sanders *et al.*, 2023).

The strong line calibrations are performed empirically from large galaxy samples. Here the oxygen abundance of the galaxies is measured using, for example, the direct T_e method and the ratios between some of the strong emission lines in the spectra are determined. A calibration between the oxygen abundance and the strong line ratios of the galaxies can then be obtained. This approach enables the estimation of the oxygen abundance for galaxies where the direct T_e method is not feasible due to undetectable auroral lines, but where other stronger emission lines are present.

Using the strong line calibrations to derive oxygen abundances comes with a number of uncertainties. First of all, they are based on empirical observations, so it should be considered whether there are significant variations between the sample of galaxies used to obtain the calibrations and the ones utilizing them. It should also be noted that some of the calibrations are double valued, meaning that a certain line ratio could have two possible oxygen abundance solutions.

Some of the most common strong emission line ratios are presented here:

$$R_3 = \frac{[OIII]\lambda5007}{H\beta} \tag{2.4}$$

$$R_2 = \frac{[OII]\lambda3727}{H\beta} \tag{2.5}$$

$$R_{23} = \frac{[OIII]\lambda5007, \lambda4959 + [OII]\lambda3727}{H\beta} \tag{2.6}$$

$$O_{32} = \frac{[OIII]\lambda5007}{[OII]\lambda3727} \tag{2.7}$$

The R_{23} and O_{32} ratios involve emission lines from both the main ionization states of oxygen (OII and OIII), hence the combined effect of these contributions can partially compensate for each other under varying ionization conditions. This is different from

the R_2 and R_3 ratios that only depend on one ionization state of oxygen (OIII). The R_3 ratio however has a small wavelength span, as the [OIII]λ5007 line and Hβ line are close in wavelength. This means that other effects, such as dust attenuation and uncertainty due to flux calibration will not have a significant impact on the ratio (Maiolino and Mannucci, 2019).

The strong line method is not a primary technique to derive the oxygen abundance but is a way to allow for an easier, albeit less precise, measure of the gas phase oxygen abundance.

2.3 Empirical scaling relations

Scaling relations are empirical relations that describe how certain observable properties of a system are related to each other. In the study of galaxies, numerous scaling relations have been observed among different galactic properties. These relations allow for a determination of properties that cannot be directly measured, and are important tools for studying how galaxies interact with their environment.

The FMR is a scaling relation that connects the interplay between the SFR, stellar mass, and oxygen abundance of galaxies (Maiolino *et al.*, 2008). To interpret this relation, it is useful to also gain insight into other scaling relations, such as the star forming main sequence (SFR-M$_*$ main sequence) and the mass-metallicity relation (MZR).

2.3.1 The star forming main sequence, SFR-M$_*$

The SFR is the rate at which new stars are being formed in a galaxy. It is typically measured in units of solar masses per year (M$_\odot$ yr^{-1}), which represents the amount of mass that is converted into stars each year in a galaxy. The process of star formation begins when dense regions of cold gas within the ISM becomes unstable and begins to collapse under their own gravity. As the gas collapses, it becomes denser and hotter, eventually reaching temperatures and densities high enough to ignite nuclear fusion reactions. This marks the beginning of a new star's life.

The SFR-M$_*$ main sequence is a scaling relation connecting the SFR and the stellar mass of actively star forming galaxies. When plotted on a log-log scale, it is an approximately

linear relation where the SFR increases with increasing stellar mass (e.g. Speagle *et al.*, 2014). Galaxies that lie above the main sequence are said to have bursty star formation, while those below the sequence have quenched star formation. The main sequence itself represents a balance between the gas supply available for star formation and the feedback processes that regulate the rate of star formation (Sparre *et al.*, 2015).

The SFR changes when the stellar mass of a galaxy changes due to a combination of factors, such as gas availability, gravitational effects, inflows and outflows, mergers, and other dynamical processes. The complex interplay between these factors also leads to a range of SFRs in galaxies at fixed masses, causing scatter in the SFR-M_* main sequence relation (Huang *et al.*, 2023). The SFR-M_* main sequence has been observed to evolve with redshift, indicating that the specific star formation, which is the star formation activity in galaxies at a given mass was higher in the past (Sparre *et al.*, 2015, Speagle *et al.*, 2014, Heintz *et al.*, 2023b, Mancuso *et al.*, 2016).

Studying the SFR-M_* main sequence and how it evolves over cosmic time, provides valuable insights into the evolutionary processes of galaxies and the underlying drivers of star formation.

2.3.2 The mass-metallicity relation, MZR

The MZR is an empirical scaling relation between the stellar mass and the gas phase oxygen abundance of galaxies (e.g. Curti *et al.*, 2020, Ma *et al.*, 2015). On a log-log scale, the relation is approximately linear, where galaxies with higher stellar masses tend to have higher oxygen abundances.

Metals are primarily produced through nucleosynthesis in stars, where the exact composition depend on the mass of the stars. The metals are then ejected into the ISM through processes like stellar winds and supernova explosions. The MZR indicates that more massive galaxies have undergone more star formation and stellar enrichment with heavy elements, resulting in a higher oxygen abundance, compared to lower mass galaxies.

The MZR is observed to be a tight correlation, but with some scatter (e.g. Ma *et al.*, 2015) due to the same effects causing the scatter in the SFR-M_* main sequence. Observations have shown that the MZR evolves with redshift, where the oxygen abundance of galaxies at a given stellar mass decrease with increasing redshift (Sanders

et al., 2021 Heintz *et al.*, 2023b), indicating that younger and less evolved galaxies, have had less time to form stars and produce metals.

The MZR provides a powerful tool for studying the chemical evolution of galaxies and understanding the processes by which heavy elements are produced and distributed throughout the universe.

2.3.3 The fundamental metallicity relation, FMR

Ellison *et al.* (2009) first discovered that galaxies with high SFRs are systematically offset to lower metal abundances than more weakly star forming galaxies at the same stellar mass. Mannucci *et al.* (2010) then studied this effect and demonstrated that the scatter in the MZR is reduced by accounting for the SFR. Mannucci *et al.* (2010) introduced the FMR, which since then has been studied extensively in different studies (e.g. Curti *et al.*, 2020, Nakajima *et al.*, 2023, Heintz *et al.*, 2023b, Andrews and Martini, 2013, Baker *et al.*, 2022).

The FMR shows that for a given stellar mass, the oxygen abundance of a galaxy decreases with its SFR. It can be represented graphically as a surface in a three-dimensional parameter space, with oxygen abundance, SFR, and stellar mass as the three axes, but can also be represented by parameterizing the second-order dependence of the MZR on SFR with a new abscissa (Mannucci *et al.*, 2010):

$$12 + log(O/H) = log(M_*) - \alpha \cdot log(SFR) \tag{2.8}$$

This relates the oxygen abundance to a linear combination of the logarithm of the stellar mass and the logarithm of the SFR, with a free parameter α. One can vary and find a value of α which minimizes the scatter of the galaxies around the FMR. The α factor is between 0 and 1 and varies across different studies. This is because the actual shape of the FMR depends on several factors, such as how galaxies are selected and how stellar masses, SFRs, and oxygen abundances are measured, all of which vary across studies.

The FMR has been predicted, as its name indicates, to be consistent across a wide range of redshifts, suggesting that it holds true for galaxies at various stages of their

evolution. This has been confirmed to be true up to redshift $z \sim 3$ (Sanders *et al.*, 2021, Mannucci *et al.*, 2010, Nakajima *et al.*, 2022). At even higher redshifts, there have previously been limited studies investigating the FMR, but with the new observations from JWST, a few studies have suggested a deviation from the FMR towards lower oxygen abundances at redshifts $z > 7$ (Heintz *et al.*, 2023b, Nakajima *et al.*, 2023, Curti *et al.*, 2023).

3 Methods

In this chapter, I will present the methods I have used, to obtain the results that I report and analyze in Chapter 4. This includes my introduction to spectroscopy by working with one-dimensional and two-dimensional spectra, using data from the MOSFIRE archive in Chapter 3.1. In Chapter 3.2, I will present my spectroscopic analysis, along with calculations of galactic properties, including the oxygen abundances of two galaxies observed with JWST: RXJ_95 at redshift $z = 9.5$ and SMACS_85 at redshift $z = 8.5$.

3.1 Introduction to spectroscopy with MOSFIRE

To become familiar with spectroscopy, I started by investigating spectroscopic data obtained with MOSFIRE. I have looked through $\sim$ 1000 two-dimensional spectra of galaxies, gathered the wavelength of each visible emission line, and converted all the two dimensional spectra into $\sim$ 300 one-dimensional spectra for each unique galaxy observation. I have lastly collected information of each galaxy observation in a catalogue.

3.1.1 Observations

MOSFIRE is an instrument located at the W. M. Keck Observatory (WMKO) on Mauna Kea, Hawaii. It observes multiple objects simultaneously, making it possible to study large regions of the sky in a relatively short amount of time. MOSFIRE's high sensitivity to faint sources, coupled with its capacity to observe infrared wavelengths, makes it well-suited for studying distant galaxies. It uses a series of aligned slits to separate the light from different objects, and then disperses the light into its component wavelengths, using gratings. The series of slits can be customized by attaching different masks, allowing for custom configurations that match specific research needs.

I have used the data obtained with MOSFIRE that is overlapping with observations obtained by the Cosmic Evolution Early Release Science (CEERS) group with JWST, indicated as the red slits (MOSFIRE) inside the blue squares (CEERS) in Figure 3.1. This data has has been obtained from the Cosmic Evolution Survey (COSMOS) field, located in the Extended Groth Strip (EGS) on the sky. The COSMOS field in the EGS region has been extensively studied by several astronomical instruments and large surveys have provided numerous datasets, making it a valuable reference area for comparison with other parts of the sky. Moreover, the field has a relatively low level of foreground extinction, which means that it is relatively free of dust and gas that can obscure observations in other parts of the sky. This makes it an ideal location for observing distant faint galaxies that can be difficult to detect.

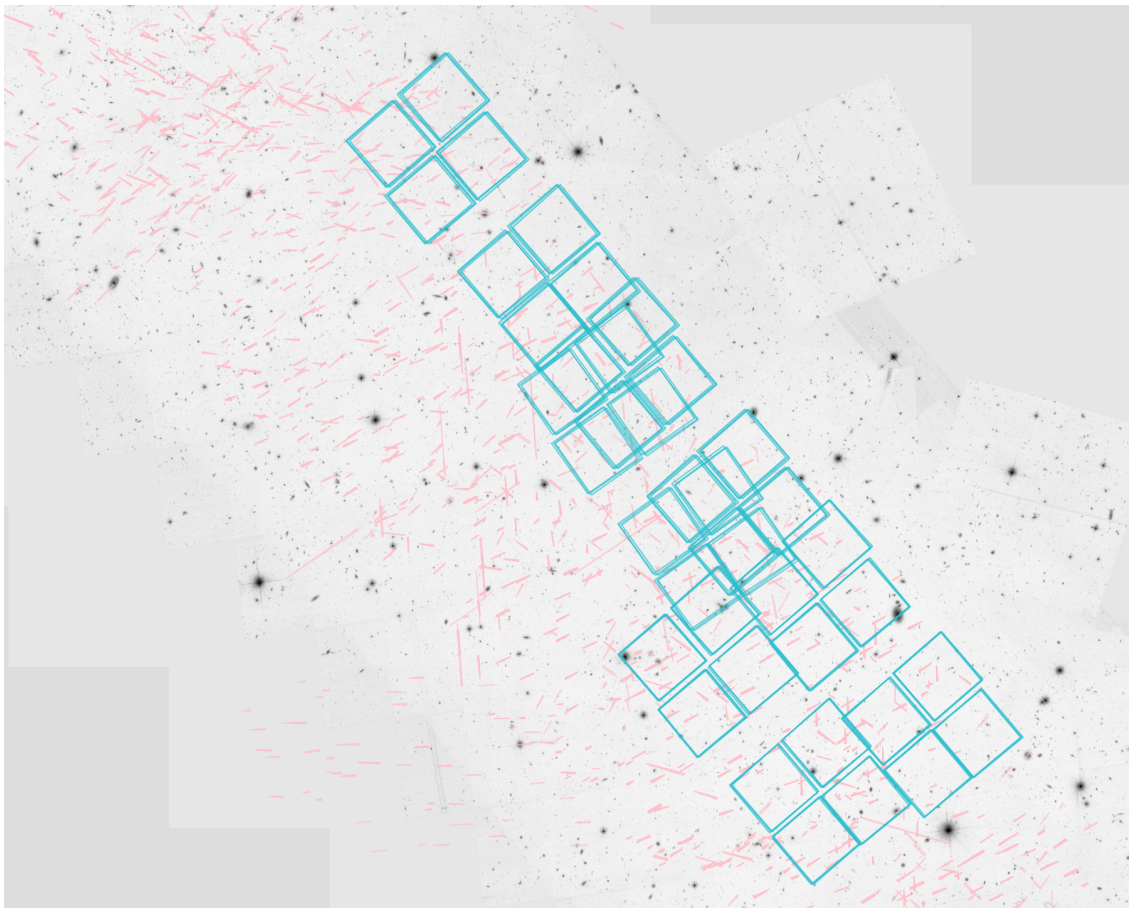

Figure 3.1: CEERS observations (blue squares) and MOSFIRE observations (red slits). I analyze observations from the red slits within the blue squares (Brammer, *CEERS and MOSFIRE observations*).

To query for the observations overlapping with the CEERS program, I have used a database provided by Gabriel Brammer (Brammer, 2022a). These data have been wavelength calibrated using known sky emission lines and fully reduced, including subtraction of bias and dark frames and flat-field correction to account for pixel-to-pixel

variations in the detector sensitivity. Also cosmic rays have been removed and there have been corrected for atmospheric dispersion. The reduction and calibration of the data closely follow the steps outlined by Valentino *et al.* (2022). Flux calibration can be done using photometry, but is challenging for such a diverse set of observations. The signal in the MOSFIRE observations I investigate has not been flux calibrated, but for the purposes in this thesis flux calibration is not required.

The MOSFIRE observations overlapping with the CEERS observations is a total of 1069 observations, with some being observations of the same galaxies captured in different bands or by different groups. I will explain how I account for this in Chapter 3.1.3.

3.1.2 Two-dimensional spectra

In the catalogue presented in Chapter 3.1.4, I have gathered the wavelength of each visible emission line in 1069 two-dimensional spectra obtained with MOSFIRE.

As the data is not flux calibrated, the signal in the spectra that I inspect corresponds to the signal to noise, which is a ratio that compares the signal of a source to the background noise. An example of a two-dimensional spectrum can be seen in Figure 3.2 (left). The emission lines are bright lines, with dark spots above and below, which are caused by nodding of the instrument. The x-axis represents the wavelengths, while the y-axis represents the offset along the slit, which also serves as a spatial indication of the location of the galaxy in the slit of observation. In Figure 3.2 (right) an example of an observation in a slit is shown. To create the two-dimensional spectra, the light is collapsed along the length of the slit, which is what corresponds to the y-axis in the spectra. In Figure 3.2 two galaxies are observed in the slit of observation: a central galaxy emitting one emission line, and a serendipitous galaxy detection on the edge of the slit, emitting three emission lines.

To examine the emission lines in each of the two-dimensional spectra I used an emission line finding code developed by a summer student, Hanga Andras-Letanovsky. The code works by investigating whether there are several pixels in a row with high signal to noise values. If so, it identifies and mark the placement of an emission line.

To ensure accurate detection of the emission lines, I visually inspected each of the 1069 spectra and marked the presence of the emission lines, using the identifications from the emission line finding code as a starting point. I wrote a program that translated

each click on an emission line in a two-dimensional spectrum into the corresponding wavelength and spatial offset. From the spatial offset, I also calculated the coordinates of the galaxy in terms of the right ascension (Ra) and declination (Dec).

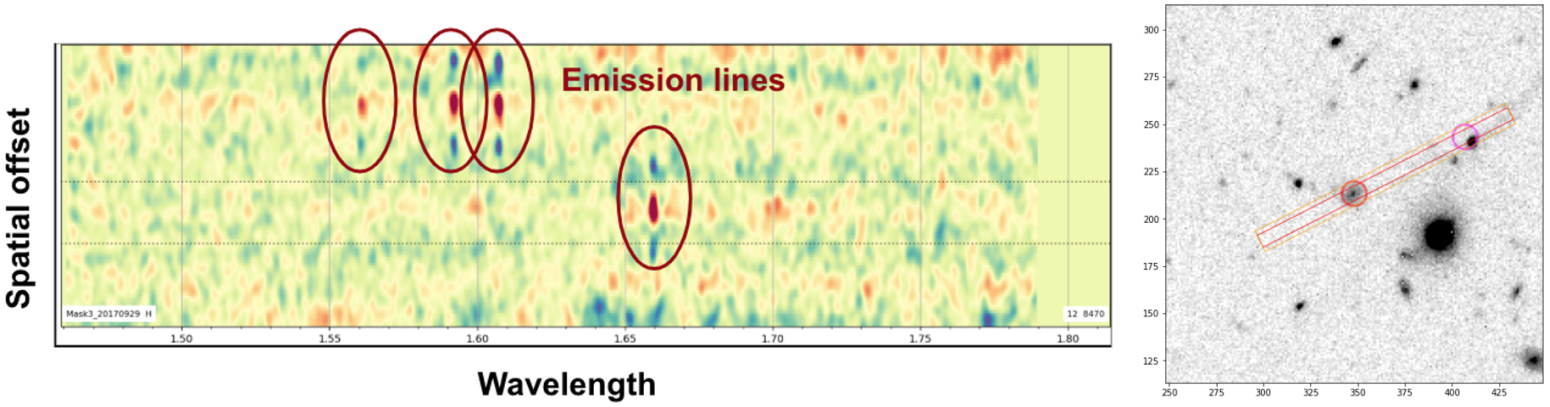

Figure 3.2: Observation of two galaxies. Left: Two-dimensional spectrum, pointing out each emission lines. Right: Slit of observation, pointing out the two galaxies (Image credit: Gabriel Brammer).

3.1.3 One-dimensional spectra

To generate the one-dimensional spectra, I grouped the 1069 total observations into 318 unique observations using their coordinates on the sky. In this way I categorized each observation of a galaxy within 0.2" of each other as the same galaxy. This process was done to ensure that all observations of the same galaxy, obtained in different bands or by different groups, were grouped together. I tested this value by visually inspecting several observations in DS9, to confirm that the galaxies were identified and grouped correctly.

I took the mean value of the spatial offsets for each galaxy and summed the spatial axis (y-axis) for each wavelength by selecting a window of 17 pixels above and below the mean value to minimize the noise, and avoid the negative spots that arise due to nodding of the instrument. I determined this window size by analyzing one of the two-dimensional spectra capturing a bright star, see Figure 3.3 (left), which can be considered as a point source. When investigating a point source, it is possible to obtain an indication of how the light gets distributed and blurred by the telescope and atmosphere. I integrated the signal along the x-axis, and determined the full-width at half-maximum (FWHM) of the positive values, see Figure 3.3 (right). The extraction value of 17 pixels, corresponds to two times the FWHM, and by choosing this value, $\sim 99\%$ of the flux is accounted for.

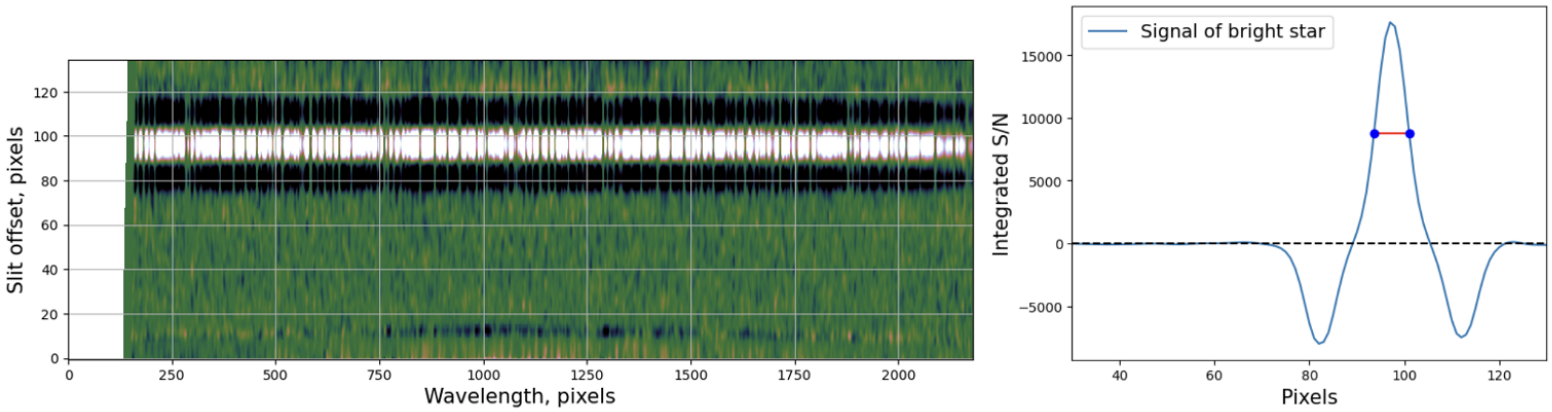

Figure 3.3: Left: Two-dimensional spectrum of a bright star. Right: The integrated signal of the star in blue, and the FWHM of the positive signal indicated in red.

In the one-dimensional spectra the summed signal to noise values are plotted against the wavelength, see upper plot in Figure 3.4. The different wavelength ranges corresponds to the various infrared wavelength bands of observations: Y (ranging from 9700 to 10007 Å), J (ranging from 11700 to 13300 Å), H (ranging from 14900 to 17800 Å), and K (ranging from 20300 to 23500 Å). For observations in the same bands, I have summed the data in quadrature.

In each observation, the slit is focused on one central galaxy, but as mentioned in Chapter 3.1.2, in few of the observations more than one galaxy has been detected. Emission lines from two different galaxies will have different spatial offsets, as seen in Figure 3.2. If both a central and a serendipitous galaxy are detected in the same observation, I have created a one-dimensional spectrum corresponding to each detection. An example of both a central and a serendipitous galaxy detection and their one-dimensional spectra can be seen in Figure 8.2.

3.1.4 The MOSFIRE catalogue

I have compiled the information of each galaxy observation into a catalogue. I have included information on whether the galaxies have emission lines or not, and if they do, the wavelength of each visible emission line. Also, there was generally a minor offset between the observed galaxy and the center of the slit. As the observed galaxies were not placed exactly at the center, I have included the observed offset from the center of the slit to the galaxies. I have also calculated a correction of the Ra and Dec coordinates given in the MOSFIRE archive, which originally corresponded to the

center of the slit. A clip of the catalogue is given in Figure 8.1, and I plan to make the catalogue public.

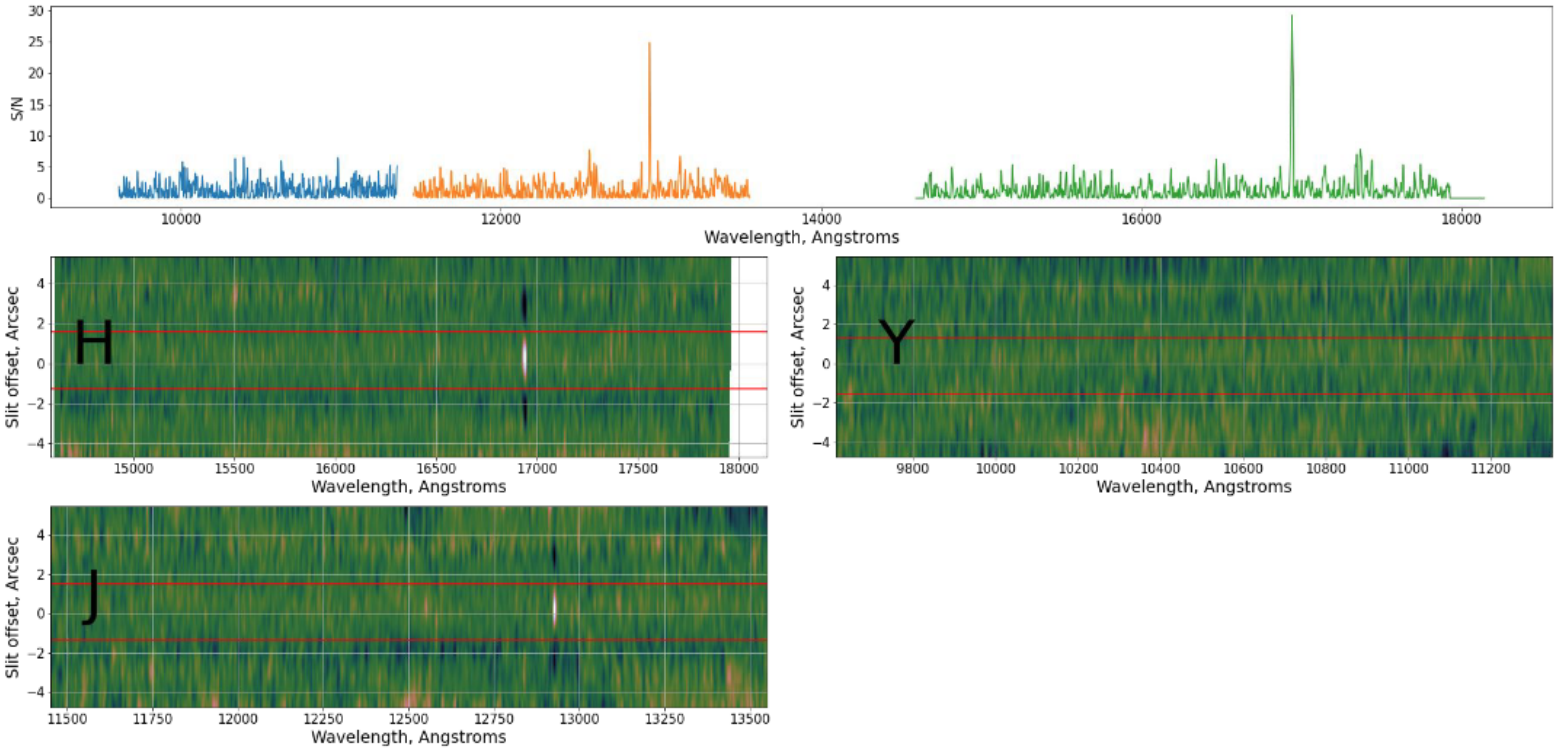

Figure 3.4: One- (above) and two- (below) dimensional spectra of a galaxy with one observable emission line, taken in three different bands of observations, Y, J and K. The red horizontal lines indicate the extraction window.

3.2 Spectroscopic properties of two high redshift galaxies

After gaining experience working with spectroscopic data from the MOSFIRE archive, I used data obtained with the JWST to investigate the chemical enrichment of high redshift galaxies, focusing specifically on spectroscopic data of the two galaxies, RXJ_95 and SMACS_85.

3.2.1 Observations and data reduction

One of the primary instruments on JWST is the Near Infrared Spectrograph (NIRSpec). NIRSpec is capable of taking spectroscopic measurements of up to 100 objects

simultaneously, using a micro-shutter array that allows it to select specific objects for observation. It covers the wavelength range of $0.6 - 5.3\ \mu m$ with different spectral resolution and observing modes (Birkmann *et al.*, 2022). The resolution of NIRSpec depends on the instrument used to disperse the light, and NIRSpec is equipped with both prism and grating systems for that purpose. The prism disperses the light over a broad wavelength range, with a changing resolution depending on the wavelength, while the gratings have a smaller wavelength range, but generally larger resolution, see Figure 3.5.

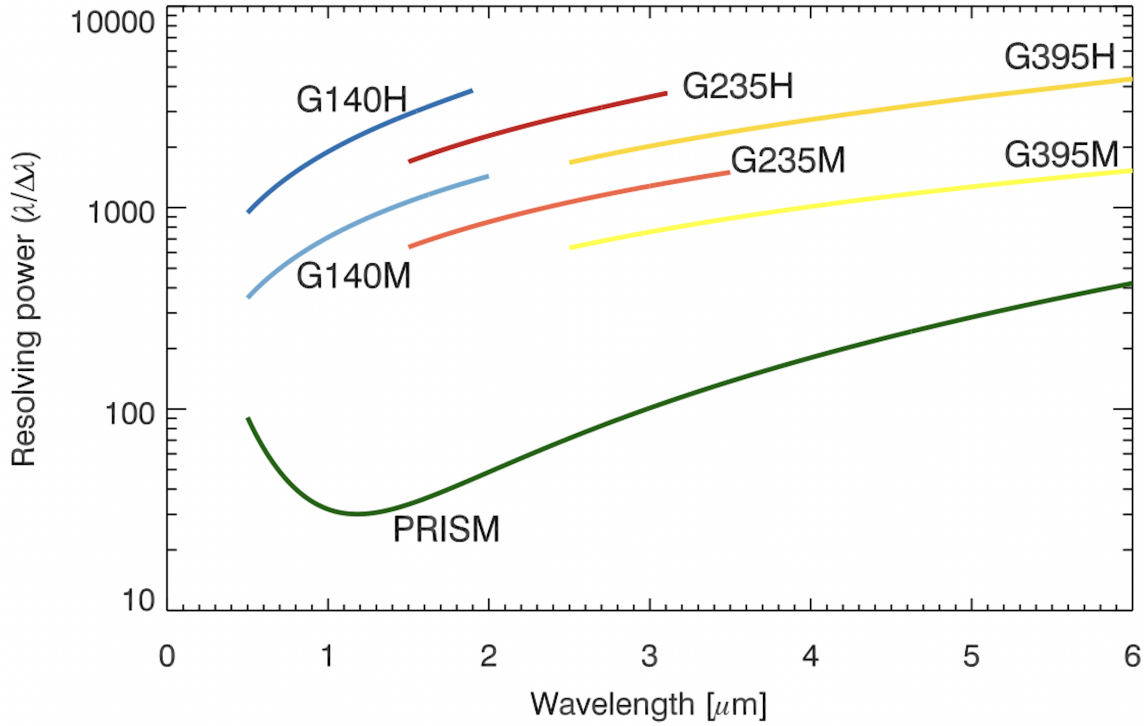

Figure 3.5: The resolving power ($\lambda/\Delta\lambda$) of NIRSpec's gratings and prism as a function of wavelength (*JWST User Documentation (JDox)* 2016).

Galaxy RXJ_95 has a redshift of $z = 9.5$ and is identified and spectroscopically confirmed as part of the Director's Discretionary program (DD-2767; PI P. Kelly) (Williams *et al.*, 2022). It is multiply imaged and highly magnified ($\mu = 19.2 \pm 3.6$ (Zitrin *et al.*, 2015)) by the foreground galaxy cluster RXJ2129 ($z = 0.234$) gravitational lens. To obtain the spectrum of RXJ_95, the NIRSpec prism has been used. The spectrum covers the full wavelength range from $0.7 - 5.2\mu m$, and can be seen in Figure 3.6 a), where I have indicated the emission lines that I will use in my analysis in red.

Galaxy SMACS_85 has a redshift of $z = 8.5$. This galaxy is from the early-release science observations (ERO) covering the SMACS J0723.3-7327 galaxy cluster ($z = 0.39$) (Liu *et al.*, 2023), and is also magnified ($\mu = 8.69 \pm 2.61$ (Harikane *et al.*, 2023)). The

spectrum of SMACS_85 is obtained using the medium-resolution gratings G235M and G395M, and covers the wavelength range from $2.7 - 5.2\mu m$ except for a gap at $4.2 - 4.5\mu m$, and can be seen in Figure 3.6 b). For both galaxies I have not plotted the first $\sim 0.3\mu m$ of the spectra, due to large noise.

The one-dimensional spectra of the galaxies RXJ_95 and SMACS_85 in Figure 3.6 has been obtained with NIRSpec and have been calibrated and reduced by Gabriel Brammer. A custom-made pipeline called msaexp (Brammer, 2022b) is used to extract and process the one-dimensional spectra from the NIRSpec exposure files. The pipeline involves several steps to ensure that the spectra are calibrated and scaled correctly for further analysis. It performs standard wavelength calibrations, by comparing the wavelengths of known spectral lines (for example from a calibration lamp) with the wavelengths detected in the data. It corrects for any non-uniformities in the detector's response to light, with flat-field calibrations and performs photometric calibrations. The flux calibration has been done by Victoria Strait and Kasper Heintz, where the overall flux densities of the spectra are scaled to the derived photometry, to match the integrated flux within the available passbands, using a wavelength-dependent polynomial function. This is important for improving the absolute flux calibration of the spectra and accounting for potential losses in flux due to the size of the slit used in the observations (Heintz *et al.*, 2023b). This scaling step is also used in the spectral energy distribution (SED) modeling of each source, which is used to derive the mass of the galaxies, described further in Chapter 3.2.8.

The photometric data used to scale the flux densities are obtained with the Near Infrared Camera (NIRCam) on JWST, which is designed to take high-resolution images of the universe in the near-infrared portion of the electromagnetic spectrum. The NIRCam observations were taken in six broad-band filters: F115W, F150W, F200W, F277W, F356W and F444W for the RXJ_95 galaxy and five filters: F150W, F200W, F277W, F356W, and F444W for the SMACS_85 galaxy. These images were also reduced and the photometric data were extracted from the catalog presented by Brammer et al. (2023, in preparation) in a similar way as described by Naidu *et al.* (2022). This has been done using the public open-source Python software package `grizli` (Brammer, 2019). `grizli` masks imaging artifacts, from potential sources of noise, some of which are outlined in Rigby (2023), and uses the Gaia DR3 catalog of known positions and motions of celestial objects, to make astrometric calibrations. `grizli` also uses a software tool called `astrodrizzle` to shift images to a common pixel scale (0.04 arcseconds per pixel). The catalog includes the most recent updated photometric zero-points, and are corrected for the Milky Way extinction. As the sources are extended in

the sky, the flux of the sources measured within an aperture size of 0.5 arcseconds in diameter is used from the catalogue (Heintz *et al.*, 2023b, Heintz *et al.*, 2023a).

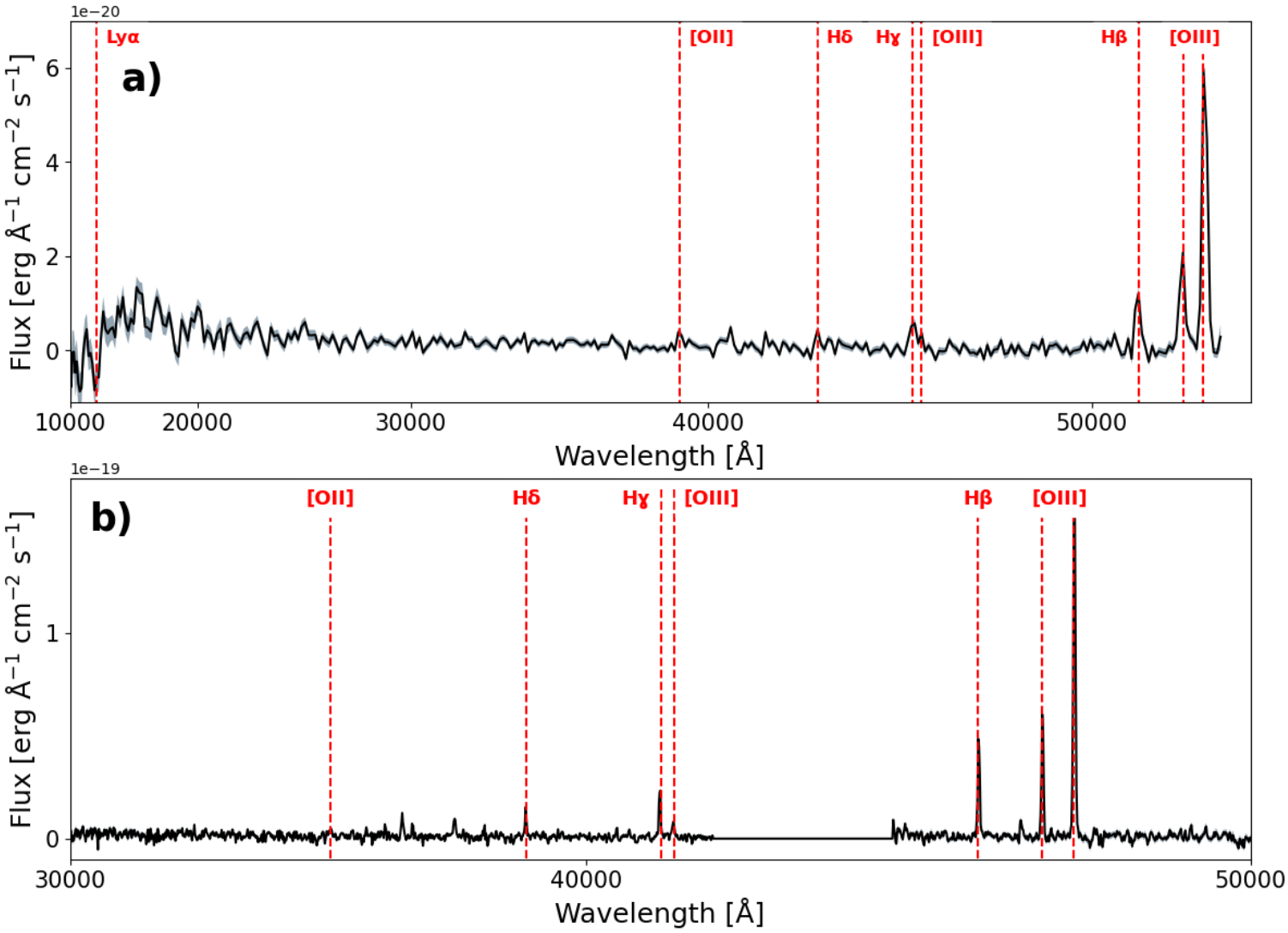

Figure 3.6: Spectra of galaxies RXJ_95 and SMACS_85. The spectra have not been corrected by the magnification factor μ, and the emission lines used in this analysis are indicated in red. a) The NIRSpec prism spectra of galaxy RXJ_95, b) The NIRSpec grating spectra (G235M and G395M) of galaxy SMACS_85.

From the two spectra in Figure 3.6, I have identified the emission lines indicated in red. As part of my spectroscopic analysis, I confirm the spectroscopic redshift and estimate the emission line fluxes. I then measure the equivalent widths of some of the lines and the SFR and the oxygen abundance of the galaxies. Throughout this work, I assume a flat cosmology with $\Omega_m = 0.315$, $\Omega_\Lambda = 0.685$ and $H_0 = 67.8 kms^{-1}Mpc^{-1}$.

3.2.2 Spectroscopic redshifts

To obtain an initial guess of the redshift of each galaxy, I have used the most prominent emission lines, in this case $H\beta$, [OIII]λ4959 and [OIII]λ5007 for both galaxies. These lines are easy to identify in the spectra due to their strong and distinct spectral features, and their close proximity in wavelength, see Figure 3.6. From the identification of these emission lines, I find the wavelength at which they are observed, and with their rest frame wavelengths available, see Table 3.1, it is possible to estimate the redshift of the galaxies, using Equation 1.1. Here I find that RXJ_95 has a redshift of $z \sim 9.5$ and SMACS_85 has a redshift of $z \sim 8.5$. After having an initial guess of the redshift, I fit the redshift simultaneously with other properties, to get a more accurate value, which I will describe in further details in Chapter 3.2.3.

Species	λ_{rest}
Lyα	1215.24
OII	3727.092
Hδ	4102.89
Hγ	4341.68
OIII	4364.436
Hβ	4862.68
OIII	4960.295
OIII	5008.240

Table 3.1: Rest frame wavelengths of spectral emission lines in vacuum in units of Ångstoms (*Table of spectral lines used in SDSS*).

3.2.3 Line fluxes

To analyze the emission lines marked with red in Figure 3.6 and their spectral properties, I have fitted a continuum model with numerous Gaussian line profiles. The Gaussian function is given by:

$$G(\lambda) = \frac{A}{\sigma\sqrt{2\pi}} e^{\frac{-(\lambda-\mu)^2}{2\sigma^2}} \tag{3.1}$$

Here A is the line flux, σ is the width of the line and μ is the center of the line, which corresponds to the wavelength at which the lines are observed.

I have used Equation 1.1 to find the placement of other lines that appear fainter in the spectra and can not be visually identified. The rest frame wavelengths of the lines, used to estimate their observed wavelengths, are given in Table 3.1. When fitting the line profiles for each transition, I require the redshift, line widths and continuum level to be fixed for all the lines, such that only the line fluxes can vary across transitions. By doing this, I am assuming that the emitting gas has similar properties and has the same velocity dispersion for all the lines. When the resolution changes across spectra, variations in line widths can also arise due to instrumental effects rather than physical phenomena. For RXJ_95 that has a prism spectrum, and thereby varying resolution with wavelength in its spectrum, the fixed line widths may not be a good assumption. An improvement would be to allow the line widths to be free or to account for the resolution changes. However, even though the resolution of the prism spectrum varies with wavelength, the emission lines I will work with are in the wavelength range from $\sim 4 - 5\mu m$, where the changes in the resolution are less than at lower wavelengths, see Figure 3.5. I also fix the line flux ratio between [OIII]λ4959 and [OIII]λ5007 to 1/3, based on the theoretical prediction of the relative transition probabilities from the excited $^1D_2$ state to $^3P_1$ and $^3P_2$ respectively, see Figure 2.1. The lines I have fitted with Gaussian line profiles and will use for further analysis are: [OII]λ3727, Hδ, Hγ, [OIII]λ4363, Hβ, [OIII]λ4959 and [OIII]λ5007, see Figure 3.6.

I have initially fitted the models with Gaussian line profiles using Python's lmfit libary, a package for least-squares minimization and curve fitting. As output I get best fit estimates of the redshift, line width, continuum level and line flux for all lines. I then combine the lmfit least squares algorithm with the Markov Chain Monte Carlo (MCMC) sampling, which can be used to explore the parameter space more thoroughly. This fitting process can be sensitive to the initial parameters used, so I use the best fit estimates I got from the first fit using least squares minimization as priors. The MCMC algorithm generates a series of samples from the posterior distribution of the parameters, which are used to estimate the mean and variance of each parameter.

Galaxy ID	[OII]λ3727	Hδ	Hγ	[OIII]λ4363	Hβ	[OIII]λ4959	[OIII]λ5007
RXJ_95	6.14 ± 1.19	5.35 ± 1.01	8.53 ± 1.20	3.62 ± 1.18	17.78 ± 1.40	30.02 ± 0.67	90.07 ± 1.96
SMACS_85	<2.21	4.57 ± 0.21	8.67 ± 0.26	2.76 ± 0.20	18.29 ± 0.33	21.67 ± 0.18	65.01 ± 0.53

Table 3.2: The derived line fluxes in units of 10^{-19} erg s^{-1} cm^{-2} with 1σ uncertainties and limits. The line fluxes have not been corrected for the magnification factor μ.

When fitting the redshift simultaneously with other properties I find that RXJ_95 has a spectroscopic redshift of $z = 9.5013 \pm 10^{-4}$ and SMACS_85 has a spectroscopic redshift of $z = 8.4956 \pm 10^{-4}$. The line fluxes and their errors are summarized in Table 3.2, and the fits are illustrated in Figure 8.3. For SMACS_85, it is not possible to separate the line intensity of the [OII]λ3727 line from the noise in the spectrum, see Figure 3.6 b). The value is therefore given as a 1σ upper limit - the highest value that a data point or measurement is expected to be with 68.27% confidence, assuming a normal distribution. I have not corrected for dust attenuation in the line fluxes, as I expect this effect to be low. I will elaborate on the reasons for this in Chapter 3.2.4 and 3.2.5.

3.2.4 Line ratios

I have computed the line flux ratios between the hydrogen lines, known as the balmer decrements, as well as other line ratio combinations, depending on the oxygen lines. I will be using these ratios to determine the oxygen abundance through strong line calibrations described in Chapter 2.2.2. The different line ratios of the two galaxies RXJ_95 and SMACS_85 can be seen in Table 3.3, with errors propagated from the line fluxes. The ratios depending on the [OII]λ3727 line for the SMACS_85 galaxy are given as upper and lower limits, as this line is detected as an upper limit in its spectrum.

I have calculated the balmer decrements: $H\gamma/H\beta$ and $H\delta/H\beta$. Assuming Case B recombination, meaning that the gas is assumed optically thin, the zero-extinction theoretical balmer decrements are $H\gamma/H\beta = 0.47$ and $H\delta/H\beta = 0.26$ (Williams *et al.*, 2022). For the galaxies RXJ_95 and SMACS_85 I find the balmer decrements to be close to the theoretical values, which suggests that there is little dust attenuation affecting the observed spectra.

Line ratios	**RXJ_95**	**SMACS_85**
$\frac{H\gamma}{H\beta}$	0.47 ± 0.08	0.47 ± 0.02
$\frac{H\delta}{H\beta}$	0.29 ± 0.06	0.25 ± 0.01
$R_3 = \frac{[OIII]\lambda5007}{H\beta}$	5.00 ± 0.39	3.55 ± 0.07
$R_2 = \frac{[OII]\lambda3727}{H\beta}$	0.34 ± 0.07	<0.12
$R_{23} = \frac{[OIII]\lambda5007,\lambda4959+[OII]\lambda3727}{H\beta}$	7.01 ± 0.56	<4.89
$O_{32} = \frac{[OIII]\lambda5007}{[OII]\lambda3727}$	14.75 ± 2.77	>29.40

Table 3.3: Ratios between line fluxes given in Table 3.2 of galaxies RXJ_95 and SMACS_85.

3.2.5 UV β slopes

The UVβ slope is a measure of the spectral energy distribution of the galaxies in the ultraviolet (UV) part of the spectrum. It is defined as the slope of the power law fit to the flux in the UV range, usually between $1250 - 2600$ Å (Calzetti *et al.*, 1994), where the flux scales as a power law with wavelength, given by:

$$F(\lambda) = A * \lambda^{\beta} \tag{3.2}$$

Where $F(\lambda)$ is the observed flux, A is a constant, λ is the wavelength and β is the slope.

The UVβ slope for RXJ_95 is listed in Table 3.5, but for SMACS_85, the wavelength range does not span to the UV range, so it has not been possible to estimate the UV slope of this galaxy. For the RXJ_95 galaxy I have used lmfit least squares algorithm to fit the power law given in Equation 3.2 to the flux in the UV range, which can be seen in Figure 8.5. The galaxy has a UVβ slope of $\beta = -1.8 \pm 0.3$, which in addition to its balmer decrements, supports a low dust attenuation (Prevot *et al.*, 1984). Dunlop *et al.* (2013) reports an average UVβ slope of $\beta = -1.8 \pm 0.6$ for galaxies at redshift $z \sim 9$, which is in agreement with that of RXJ_95. Bhatawdekar and Conselice (2021) however finds a bluer value of $\beta = -2.51 \pm 0.3$ for galaxies at $z \sim 9$.

3.2.6 Equivalent widths

The equivalent width of an emission line is a measure of the strength of the line, and is defined as the width of the spectral continuum that has the same area as the line. More specifically, it is the integral of the flux density of the line divided by the continuum flux density, over the wavelength range of the line, given by:.

$$EW = \int_a^b \left(1 - \frac{F_{line}}{F_{cont}}\right) d\lambda \tag{3.3}$$

Where F_{line} is the flux of the line with a wavelength range spanning from a to b and F_{cont} is the flux of the continuum.

Galaxy ID	EW(Hβ)	EW(OIIIλ4959)	EW(OIIIλ5007)
RXJ_95	252^{+26}_{-22}	407^{+42}_{-35}	1134^{+118}_{-98}
SMACS_85	160^{+11}_{-9}	186^{+13}_{-11}	582^{+39}_{-35}

Table 3.4: Rest frame equivalent widths (EW) of Hβ, [OIII]λ4959 and [OIII]λ5007 in units of Ångstoms.

I have calculated the equivalent widths of the three brightest lines, Hβ, [OIII]λ4959 and [OIII]λ5007 for the two galaxies. To account for variations in the continuum, I have fitted a continuum model with these three line profiles only, which can be seen in Figure 8.3. The rest frame equivalent widths of the lines (the equivalent widths divided by a factor (1+z)) are given in Table 3.4, together with their associated errors propagated from errors on the line fluxes. I will use these in Chapter 4.1 to verify my choice of strong line calibration, when determining the oxygen abundance.

3.2.7 Star formation rates

I infer the SFR, for each galaxy based on the Hβ line flux measurement, using following equation (Kennicutt, 1998):

$$SFR_{H\beta}(M_{sun}/yr) = 5.5 \cdot 10^{-42} L_{H\beta}(erg/s) \cdot f_{H\alpha/H\beta} \tag{3.4}$$

Here a Kroupa initial mass function (IMF) has been assumed, which is a powerlaw function broken into three segments, low-mass stars, intermediate-mass stars, and high-mass stars, that describes the distribution of masses for newly formed stars in a given population (Kroupa, 2001). The theoretical $f_{H\alpha/H\beta}$ ratio is 2.86 from the Case B recombination model at $T_e = 10^4$ K (Osterbrock and Ferland, 2006) and $L_{H\beta}(erg/s)$ is the luminosity based on the flux of the $H\beta$ line, given by:

$$L_{H\beta}(erg/s) = f_{H\beta}(ergs^{-1}cm^{-2})4\pi D_L^2 \tag{3.5}$$

Here $f_{H\beta}$ is the line flux of $H\beta$ and D_L is the luminosity distance. I use the cosmology distance calculator from `astropy` (Robitaille *et al.*, 2013) to infer the luminosity distances D_L to the given redshifts of the two galaxies.

The statistical uncertainties from the Hβ line flux measurements are typically $10-30\%$, whereas the uncertainties from the choice of the IMF typically is $20-30\%$. I therefore conservatively assume a 0.4 dex total uncertainty in following analysis for each SFR measurement (Heintz *et al.*, 2023b). The $SFR_{H\beta}$ for the two galaxies is given in Table 3.5.

Galaxy ID	z_{spec}	$SFR_{H\beta}$ [$M_\odot$ yr^{-1}]	log M_* [$M_\odot$]	μ	UVβ slope
RXJ_95	9.5013 $\pm 10^{-4}$	$1.7^{+0.2}_{-1.0}$	7.6 $\pm$ 0.2	19.2 $\pm$ 3.6	-1.8 $\pm$ 0.3
SMACS_85	8.4956 $\pm 10^{-4}$	$3.0^{+4.5}_{-1.8}$	7.6 $\pm$ 0.4	8.7 $\pm$ 2.6	-

Table 3.5: The spectroscopic redshift (z_{spec}), SFR based on the Hβ line flux measurement ($SFR_{H\beta}$), logarithm to the stellar mass ($logM_*$), magnification factor (μ) and $UV\beta$ slope. The SFRs and stellar masses have been corrected for the magnification factor.

3.2.8 Stellar masses

Photometry from NIRCam, is used to constrain the stellar mass of the two galaxies. In this work I will use the stellar mass of the RXJ_95 galaxy obtained by Heintz *et al.* (2023b) and the stellar mass of SMACS_85 obtained by Heintz *et al.* (2023a). These stellar masses are given in Table 3.5.

To infer the stellar mass of the galaxies, SEDs have been modelled using the fitting code `Bagpipes` (Carnall *et al.*, 2018). The code generates model SEDs based on input priors, which are then compared to the observed SED. By utilizing MCMC optimization a range of posteriors of physical parameters that describe the galaxy, including the stellar mass are determined. The modeling incorporates stellar population models, star formation history (SFH), nebular emission, dust attenuation, initial mass function (IMF), and metallicity.

For the SMACS_85 galaxy, Heintz *et al.* (2023a) finds a stellar mass of $\log(M_*/M_\odot) = 7.15 \pm 0.15$. However, Giménez-Arteaga *et al.* (2022) finds a substantially higher stellar mass of $\log(M_*/M_\odot) \sim 8$, based on a resolved SED study on a set of galaxies at $z \geq 5$ (including SMACS_85), which has been recovered assuming a burstier SFH (Tacchella *et al.*, 2022). To take this into account and any potential systematic uncertainties on the stellar mass estimates from varying SFH models and in general across SED fitting codes, Heintz *et al.* (2023a) assume a stellar mass with conservative uncertainties of $log(M_*/M_\odot) = 7.2 - 8.0$. I therefore assume a stellar mass of $log(M_*/M_\odot) = 7.6 \pm 0.4$ in the following analysis.

For RXJ_95, Heintz *et al.* (2023b) finds a stellar mass of $log(M_*/M_\odot) = 7.56 \pm 0.08$. For this galaxy I have applied an additional 0.2 dex uncertainty to the statistical error on the derived stellar masses in the following analysis, due to the systematic uncertainties stemming from the exact choice of SED modelling technique used (Heintz *et al.*, 2023b).

3.2.9 Oxygen abundances

As described in Chapter 2.2.1, the electron temperature of the ionized gas in a galaxy, can be used to derive the oxygen abundance. The [OIII]λ4363/([OIII]λ4959+λ5007) ratio is sensitive to the electron temperature of the ionized gas as the excitation energy of the [OIII]λ4363 line is higher than that of the [OIII]λ4959 and [OIII]λ5007 lines. The ratio increases as the electron temperature increases, making it a sensitive indicator of the electron temperature of the ionized gas. Both the RXJ_95 and SMACS_85 spectra show detection of the auroal line [OIII]λ4363, which is indicated in Figure 3.6. This allows me to determine the oxygen abundance using the direct T_e method for the two galaxies.

An analytical solution can be worked out for the electron temperature and the oxygen abundance, based on the atomic physics described in Chapter 2.2.1. Following the iterations outlined by Izotov *et al.* (2006), I will use following equation to estimate the electron temperature:

$$t = \frac{1.432}{log[(\lambda 4959 + \lambda 5007)/\lambda 4363] - log(C_T)} \tag{3.6}$$

Here $t = 10^{-4}T_e$ where T_e is the electron temperature, $x = 10^4 N_e t^{-0.5}$ where N_e is the electron density and C_T is given by:

$$C_T = (8.44 - 1.09t + 0.5t^2 - 0.08t^3)\frac{1 + 0.0004x}{1 + 0.044x} \tag{3.7}$$

In general, the electron density N_e is less than 10^4 cm^{-3}, for the ionized HII regions in galaxies, so in principle, the term containing x is never important, see Chapter 2.2.1.

I derive the oxygen abundance from the electron temperature and the flux of the oxygen emission lines to the flux of the hydrogen lines arising due to recombination ([O$^+$]/H$^+$ and [O^{2+}]/H$^+$), using following equations (Izotov *et al.*, 2006):

$$12 + logO^+/H^+ = log\frac{\lambda 3727}{H\beta} + 5.961 + \frac{1.676}{t} - 0.40logt - 0.034t + log(1 + 1.35x) \tag{3.8}$$

$$12 + logO^{2+}/H^+ = log\frac{\lambda 4959 + \lambda 5007}{H\beta} + 6.200 + \frac{1.251}{t} - 0.55logt - 0.014t, \tag{3.9}$$

where O^+ is the singly ionized oxygen (OII), O^{2+} is the doubly ionized oxygen (OIII) and H^+ is ionized hydrogen.

Assuming that all oxygen atoms are ionized, but not more than doubly ionized, adding the oxygen abundances of Equations 3.8 and 3.9, represents the total oxygen abundance in the galaxy:

$$O/H = O^{2+}/H^{+} + O^{+}/H^{+} \tag{3.10}$$

I solve for the oxygen abundance as a function of electron temperature and density using Equation 3.6, 3.8, 3.9 and 3.10, which is illustrated in Figure 3.7 for RXJ_95 (Heintz *et al.*, 2023b). The same solution for SMACS_85 is shown in Figure 8.4. For SMACS_85, the [OII]λ3727 line is not detected in the spectrum and is given as a 1σ upper limit in Table 3.2. Therefor I have not included the term O^{+}/H^{+} from Equation 3.8 when deriving the total oxygen abundance of SMACS_85. This is reasonable, as the O^{2+}/H^{+} term will be the dominant one, which is also seen for RXJ_95 in Figure 3.7. I have included the term containing the density, to illustrate that the electron temperature and oxygen abundance is not affected by a changing electron density, as long as it is below $N_e \sim 10^4$ cm^{-3}.

Assuming electron densities below $N_e \sim 10^4$ cm^{-3}, I find an electron temperature of $T_e = (2.2 \pm 0.7) \cdot 10^4 K$ for RXJ_95, and $T_e = (2.3 \pm 0.2) \cdot 10^4 K$ for SMACS_85.

I infer uncertainties on the temperature measurements, from the relative error of the line ratio in Equation 3.6: $(\lambda 4959 + \lambda 5007)/\lambda 4363$. For the oxygen abundances, I estimate the uncertainties to be the same as the relative error of the line ratio in Equation 3.9: $(\lambda 4959 + \lambda 5007)/H\beta$, as this term is the dominant term in Equation 3.10. The obtained oxygen abundances using the direct T_e method is given in Table 4.1.

As described in Chapter 2.2.2, the oxygen abundance can also be determined in a less precise, but in many cases more approachable method through strong line calibrations, that have been obtained from large galaxy samples in the local universe. Using these calibrations, the oxygen abundance can be determined for galaxies where the auroral line is not resolved in their spectra.

I will be using the line ratios mentioned in Chapter 2.2.2 and given in Table 3.3 to also determine the oxygen abundance through strong calibrations. In Figure 4.1, I have plotted different strong line calibration, made by different studies (Curti *et al.*, 2017, Curti *et al.*, 2020, Maiolino *et al.*, 2008, Bian *et al.*, 2018, Nakajima *et al.*, 2022). For further analysis, and to obtain the oxygen abundances, I will use the calibration from Nakajima *et al.* (2022) for EW(Hβ) > 200Å, plotted as the blue line in Figure 4.1 with scatter. This calibration seems to fit my results obtained using the direct T_e method

best, and I will expand on this in Chapter 4.1. The obtained oxygen abundances using the strong line calibrations from Nakajima *et al.* (2022) is given in Table 4.1.

The errors on the oxygen abundance values obtained using the strong line calibrations, I have estimated from the errors on the line ratios. I have also added 0.1, which Nakajima *et al.* (2022) states as the 1σ logarithmic uncertainty on the oxygen abundance for a given line ratio, when using the calibration for EW(Hβ) > 200Å.

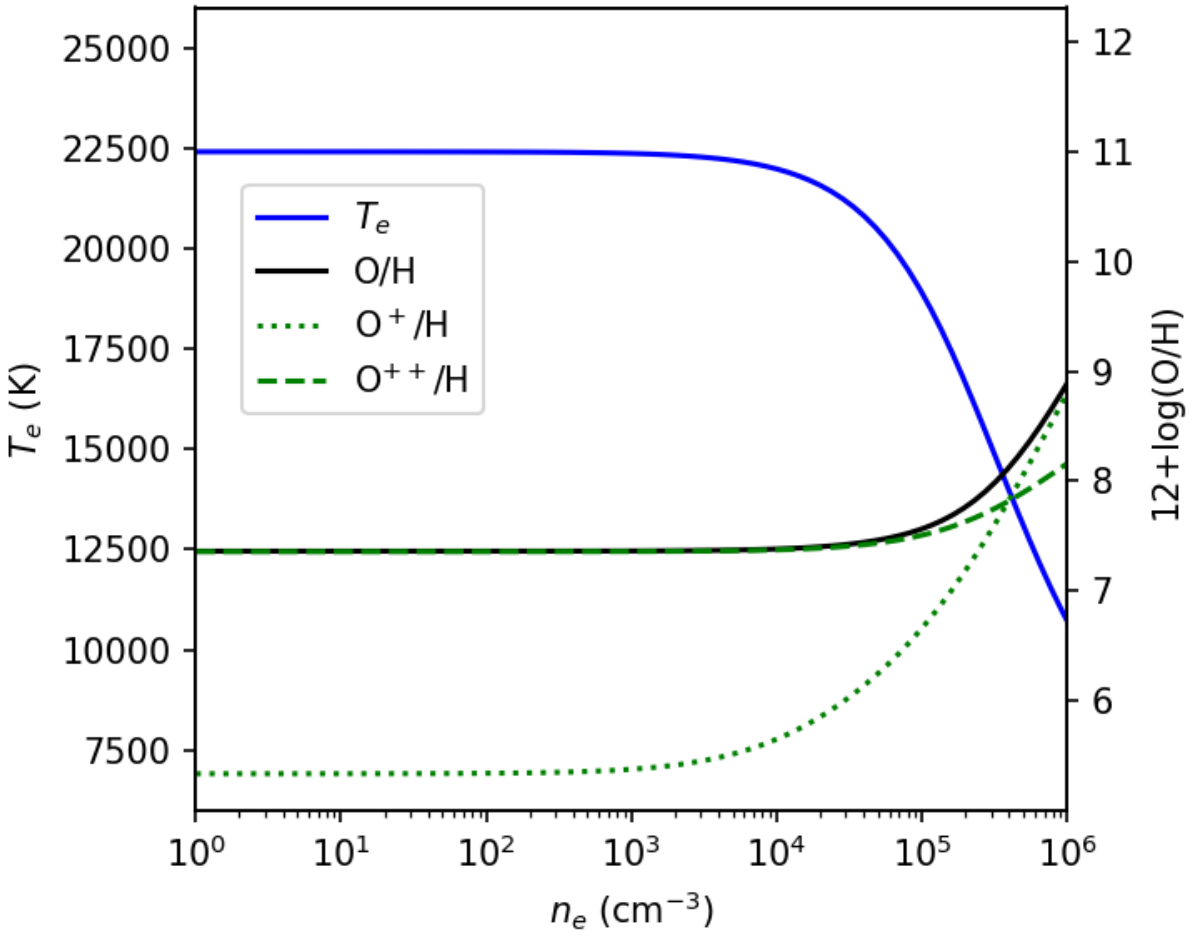

Figure 3.7: Recreated figure from Heintz *et al.* (2023b) of the derived electron temperature T_e and the oxygen abundance $12 + log(O/H)$ for galaxy RXJ_95 as a function of the electron density n_e. The same solution for SMACS_85 is shown in Figure 8.4.

4 Results and Analysis

In this chapter, I will present the results of the oxygen abundance measurements I have gained using the implementations described in Chapter 3. I will compare these results to empirical scaling relations obtained by different studies described in Chapter 2.3.

4.1 Oxygen abundance measurements

To determine the oxygen abundance of the two galaxies RXJ_95 and SMACS_85, I have utilized the direct T_e method. I obtain a value of 7.36 ± 0.08 for RXJ_95 and 7.19 ± 0.02 for SMACS_85. The oxygen abundances for the two galaxies are presented in Table 4.1. Additionally, for comparison purposes I have used the strong line calibrations from Nakajima *et al.* (2022) to calculate the oxygen abundance, and I will explain my choice of calibration below.

In Figure 4.1, I have plotted the different strong line calibrations obtained by Nakajima *et al.* (2022), Bian *et al.* (2018), Maiolino *et al.* (2008) and Curti *et al.* (2017). The strong line ratios used for these calibrations are R_3, R_{23}, R_2 and O_{32}, which each are given and explained in Chapter 2.2.2. In Figure 4.1, I have also plotted the oxygen abundances that I find by using the direct T_e method for the two galaxies and their corresponding line ratios given in Table 3.3. Since these values align best with the calibrations from Nakajima *et al.* (2022) for EW(Hβ) > 200Å, and the majority of them lie within the scatter of the calibrations, I have used these calibrations to derive the oxygen abundances through the strong line calibration method. The Hβ equivalent widths that I measure for the two galaxies can be seen in Table 3.4. For RXJ_95, the Hβ equivalent width is $EW(H\beta) = 252^{+26}_{-22}$, which is larger than 200Å. For SMACS_85, I find the Hβ equivalent width to be $EW(H\beta) = 160^{+11}_{-9}$. Although this value is below 200Å, the oxygen abundance data points for SMACS_85 still seem to align best with the calibration from Nakajima *et al.* (2022) for Hβ equivalent widths greater than 200Å.

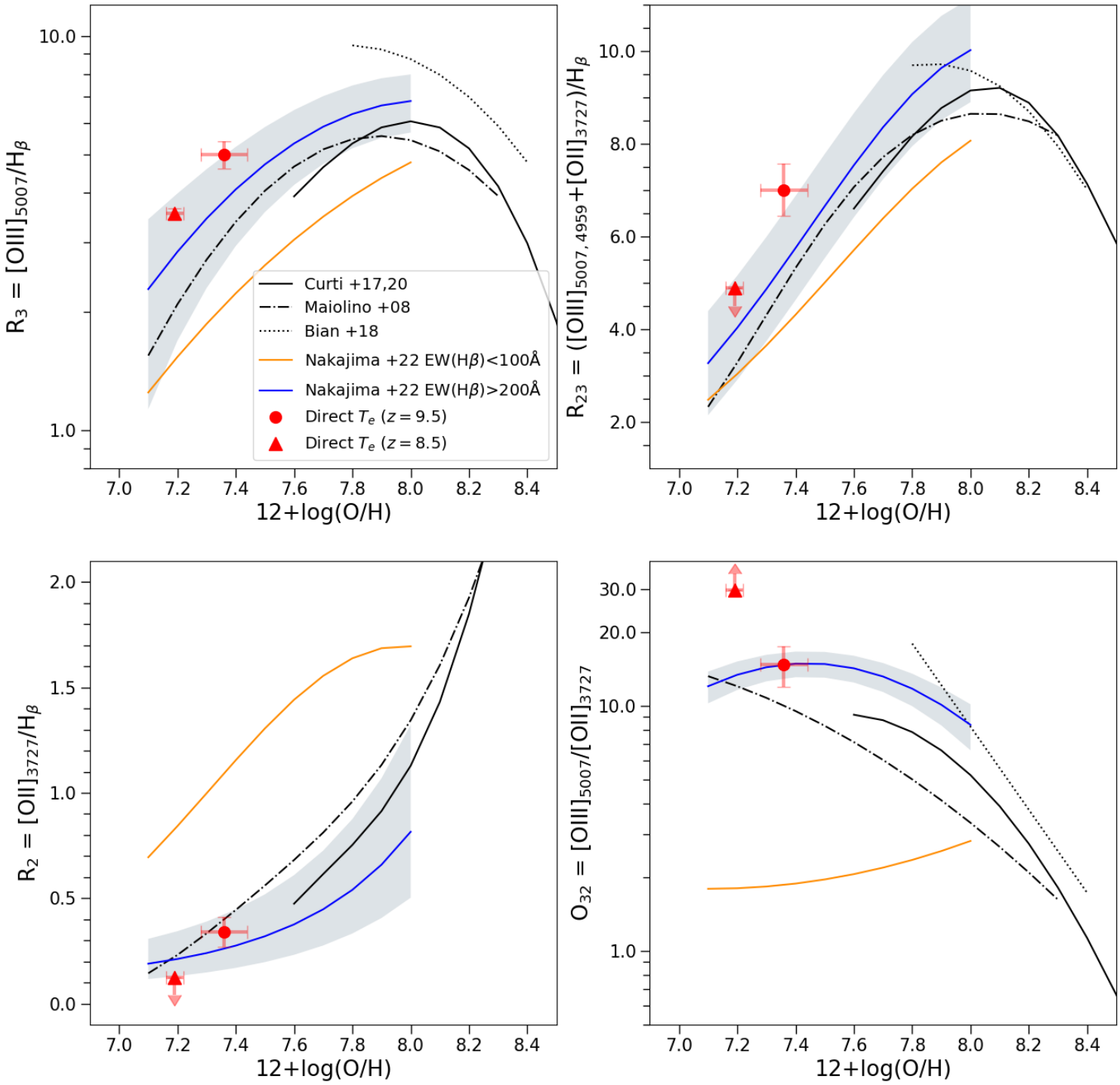

Figure 4.1: Plot of different strong line calibrations (Nakajima *et al.*, 2022, Bian *et al.*, 2018, Maiolino *et al.*, 2008, Curti *et al.*, 2017). For the calibration by Nakajima *et al.* (2022) with EW(Hβ) $>$ 200Å, the 1σ scatter of the calibration is plotted. The oxygen abundances obtained using the direct T_e method and corresponding line ratios of galaxies RXJ_95 and SMACS_85 are indicated by red data points with error bars.

The oxygen abundances obtained using the strong line calibrations are listed in Table 4.1. For both galaxies, the oxygen abundances obtained through the direct T_e method is lower than those obtained through the strong line calibrations. However, it should be noted that the uncertainties on the oxygen abundances using the strong line calibrations are larger, and within the uncertainties of these, the oxygen abundance measurements using the two different methods are consistent with each other. For the RXJ_95 galaxy, the oxygen abundances calculated using the strong line calibrations are consistent across different strong line ratios. What should be noticed, is that it is not possible to obtain an upper limit on the oxygen abundance using the O_{32} calibration, as the upper limit on this line ratio has no solution to the calibration. For SMACS_85 I find upper limits on the oxygen abundance using the R_{23} and R_2 calibrations, as the [OII]λ3727 line is not detected in the spectrum. I find that there is no solution for the oxygen abundance using the O_{32} calibration. While the oxygen abundance calculated using the calibrations with the R_3 and R_{23} ratios are consistent, the oxygen abundance calculated using the R_2 ratio show strong deviation. The use of the R_2 and O_{32} calibrations to determine the oxygen abundance is unreliable for SMACS_85 because of the ratios strong dependence on the undetected [OII]λ3727 line.

Galaxy ID	T_e method	R_3	R_{23}	R_2	O_{32}
RXJ_95	7.36 ± 0.08	$7.5^{+0.2}_{-0.2}$	$7.5^{+0.2}_{-0.2}$	$7.5^{+0.4}_{-0.5}$	$7.5_{-0.7}$
SMACS_85	7.19 ± 0.02	$7.3^{+0.2}_{-0.2}$	< 7.3	< 6.3	–

Table 4.1: Oxygen abundance measurements obtained through the T_e method and the strong line calibrations from Nakajima *et al.* (2022) for EW(Hβ)>200Å. The ratios are defined in Chapter 2.2.2.

For further analysis, I have chosen to use the oxygen abundance obtained from the R_3 ratio. This relation has a small empirical scatter and is supported by recent theoretical frameworks and empirical constraints based on oxygen abundances estimates through the direct T_e method (Nakajima *et al.*, 2022, Nakajima *et al.*, 2023). The R_3 ratio depends on the [OIII]λ5007 and Hβ lines that are clearly detected in both the RXJ_95 and SMACS_85 spectra, and it doesn't depend on the O[II]λ3727 line, which is not detected in the SMACS_85 galaxy spectrum. Even though the R_3 ratio only depends on one ionization state of oxygen (OIII), this state will be the dominant state at the given electron densities and temperatures, see Figure 3.7. Moreover, the RXJ_95 galaxy has a prism spectrum, causing the resolution to change over a wide wavelength range, as described in Chapter 3.2.1. The R_3 ratio has a small wavelength range, so when using

this line ratio, it introduces less uncertainty in the flux calibration, resulting in less uncertainty in the oxygen abundance. Additionally, a small wavelength range at higher wavelengths, such as for the [OIII]λ5007 and Hβ lines in the R_3 ratio, is less affected by dust attenuation, even though I do not expect this effect to be significant for the galaxies RXJ_95 and SMACS_85 due to their balmer decrements being close to the theoretical values for zero dust extinction, see Chapter 3.2.4.

4.2 Comparison to the SFR-M_* main sequence

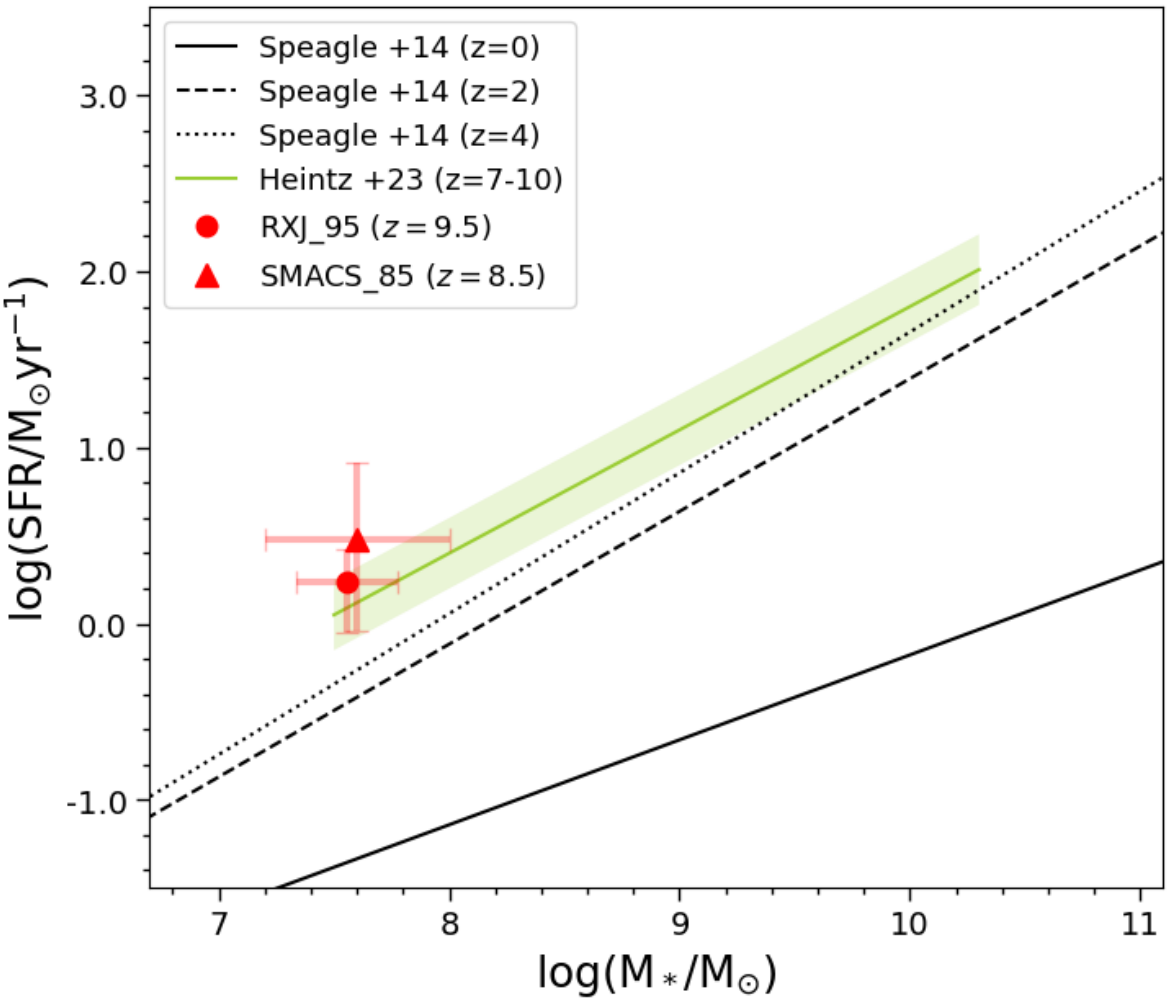

Figure 4.2: The SFR-M_* main sequence by Speagle *et al.* (2014) is plotted at redshifts $z = 0$, $z = 2$, and $z = 4$, and by Heintz *et al.* (2023b) at redshifts $z = 7 - 10$. The scatter of the relation by Heintz *et al.* (2023b) is 0.4 dex, and added to the relation. The galaxies RXJ_95 and SMACS_85 at $z = 9.5$ and $z = 8.5$ respectively is also plotted in red with errorbars.

To examine the oxygen abundances of RXJ_95 and SMACS_85 and how they compare to the FMR, which links the oxygen abundance to the stellar mass and SFR of galaxies, I will initially focus on analyzing the relation between the SFR and stellar mass through the SFR-M_* main sequence, which is described in detail in Chapter 2.3.1. I have utilized the SFR-M_* main sequences obtained by Speagle *et al.* (2014) and Heintz *et al.* (2023a), that both find an increase in SFR when the stellar mass of galaxies increases, as illustrated in Figure 4.2. The research by Speagle *et al.* (2014) examined the SFR-M_* main sequences relation at redshifts $z = 0$, $z = 2$, and $z = 4$, while the research by Heintz *et al.* (2023a) examined the relation at redshift $z = 7 - 10$. Both Speagle *et al.* (2014) and Heintz *et al.* (2023a) find that for a given mass the SFR increases with redshift. This is consistent with the galaxies RXJ_95 and SMACS_85, as they lie above the SFR-M_* main sequences obtained by Speagle *et al.* (2014), and are consistent with the relation obtained by Heintz *et al.* (2023b) with a scatter of 0.4 dex within 1σ.

4.3 Comparison to the MZR

I have examined The MZR, which is described in more detail in Chapter 2.3.2. In Figure 4.3, I have plotted relations obtained by various researchers, investigating at different redshifts (Curti *et al.*, 2020, Andrews and Martini, 2013, Sanders *et al.*, 2021, Heintz *et al.*, 2023b). Also, I have plotted the oxygen abundances found using both the direct T_e method (in red) and the strong line calibration method (in grey) for RXJ_95 and SMACS_85. For each of the MZRs plotted, the oxygen abundance increases with increasing stellar mass. Moreover the MZRs plotted show that as the redshift increases, the oxygen abundance tends to decrease for a given stellar mass. The decrease in oxygen abundance for a given mass with redshift, is in agreement with the findings from my analysis of RXJ_95 and SMACS_85. For the oxygen abundances obtained using the strong line calibrations and the the direct T_e method, both galaxies RXJ_95 and SMACS_85 seem to agree with the relation obtained by Heintz *et al.* (2023b) with a scatter of 0.3 dex within 1σ. When comparing the galactic properties of RXJ_95 and SMACS_85 to the SFR-M_* main sequence and the MZR obtained by Heintz *et al.* (2023b), it should be noted that the galaxy RXJ_95 was part of the galaxy sample used to obtain these relations.

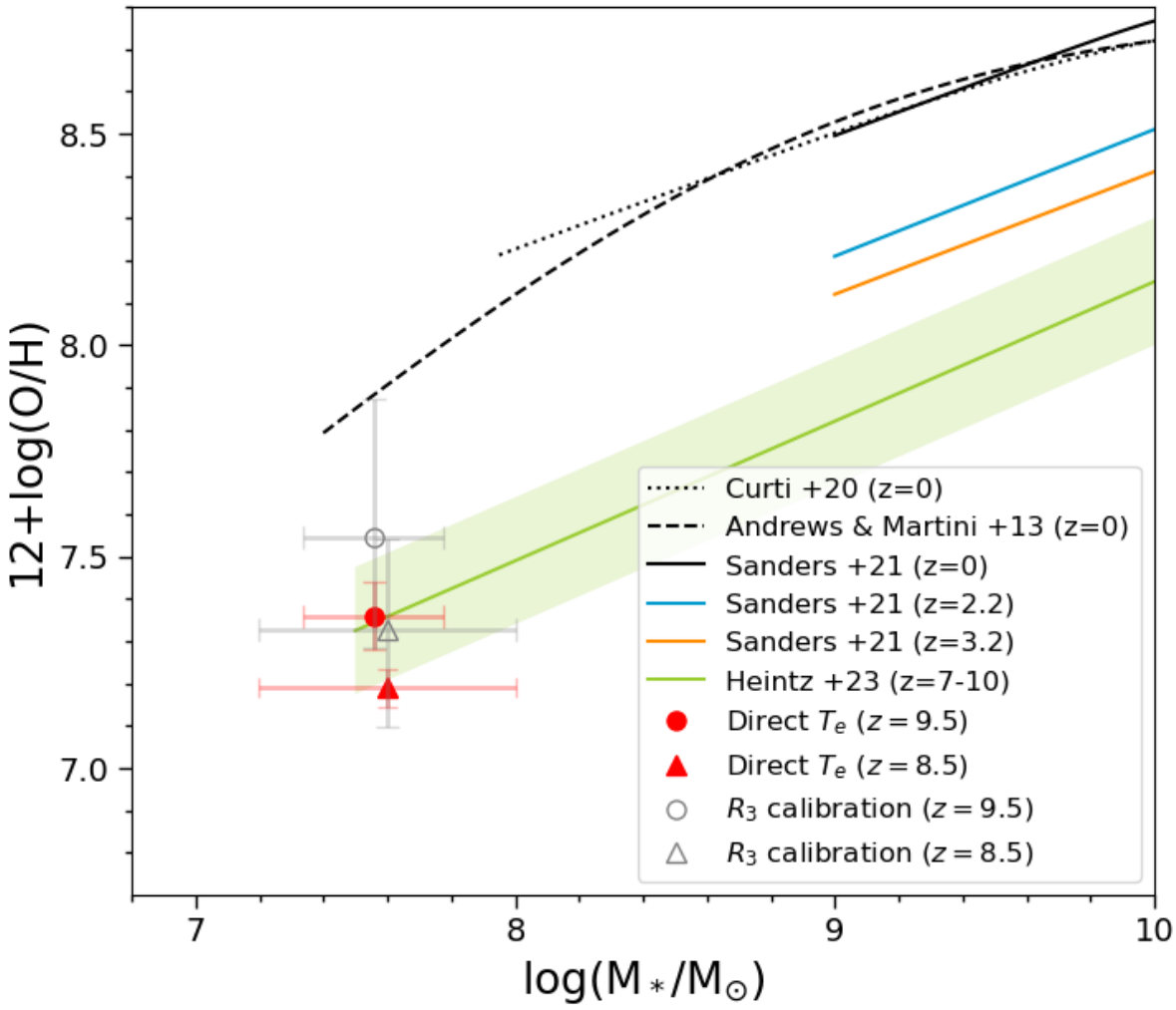

Figure 4.3: The MZR obtained by Curti *et al.* (2020), Andrews and Martini (2013), Sanders *et al.* (2021) and Heintz *et al.* (2023b), at different redshifts. The scatter of the relation by Heintz *et al.* (2023b) is 0.3 dex, and added to the relation. The galaxies RXJ_95 and SMACS_85 at $z = 9.5$ and $z = 8.5$ respectively are also shown. Here the red points with errorbars are the oxygen abundances obtained using the direct T_e method and the grey points are the oxygen abundances obtained using strong line calibrations.

4.4 Comparison to the FMR

The stellar mass, metal abundance, and SFR of galaxies are shown to have a tight correlation in the local universe, related by the FMR (Mannucci *et al.*, 2010, Curti *et al.*, 2020, Andrews and Martini, 2013, Kashino *et al.*, 2016, Troncoso *et al.*, 2014), which is described in more detail in Chapter 2.3.3. In Figure 4.4 I have plotted the FMR predicted by Curti *et al.* (2020) and Andrews and Martini (2013), who both use an α factor of $\alpha = 0.66$. Specifically, Curti *et al.* (2020) uses this factor for the sample

of galaxies with a specific star formation rate (sSFR) greater than $10^{-9.5}$ yr^{-1}. The sSFR is defined as the SFR of a galaxy divided by its stellar mass: $sSFR = SFR/M_*$. For RXJ_95 and SMACS_85, their sSFR values are of the order of $\sim 10^{-8}$ yr^{-1} and $\sim 10^{-7}$ yr^{-1}, respectively. Therefore, I have used a factor of $\alpha = 0.66$ for RXJ_95 and SMACS_85, which are plotted as well in Figure 4.4, both for the oxygen abundances found using the direct T_e method (in red) and using the strong line calibration method (in grey). As these galaxies have lower masses and higher SFRs than the samples from Andrews and Martini (2013) and Curti *et al.* (2020), I have extrapolated their relations towards lower masses and higher SFRs, which I will discus further in Chapter 5.4. The oxygen abundances found from the strong line calibrations, are in agreement with the FMR from Andrews and Martini (2013) within 1σ. However, for the oxygen abundances found from the direct T_e method, the measurements lie significantly below the FMRs obtained by Curti *et al.* (2020) and Andrews and Martini (2013). Specifically, for RXJ_95 the oxygen abundances obtained using the direct T_e method lie $\sim 4\sigma$ below the FMR obtained by Andrews and Martini (2013), while it for SMACS_85 lie more than 10σ below. Both lie even further below the more newly predicted FMR by Curti *et al.* (2020). Additionally, in Figure 4.4 I have plotted results from Nakajima *et al.* (2023) of galaxies at redshift $z = 4 - 7$, that also uses an α factor of $\alpha = 0.66$. Nakajima *et al.* (2023) finds that their results are in agreement with the FMR obtained by Andrews and Martini (2013) at redshifts $z < 8$.

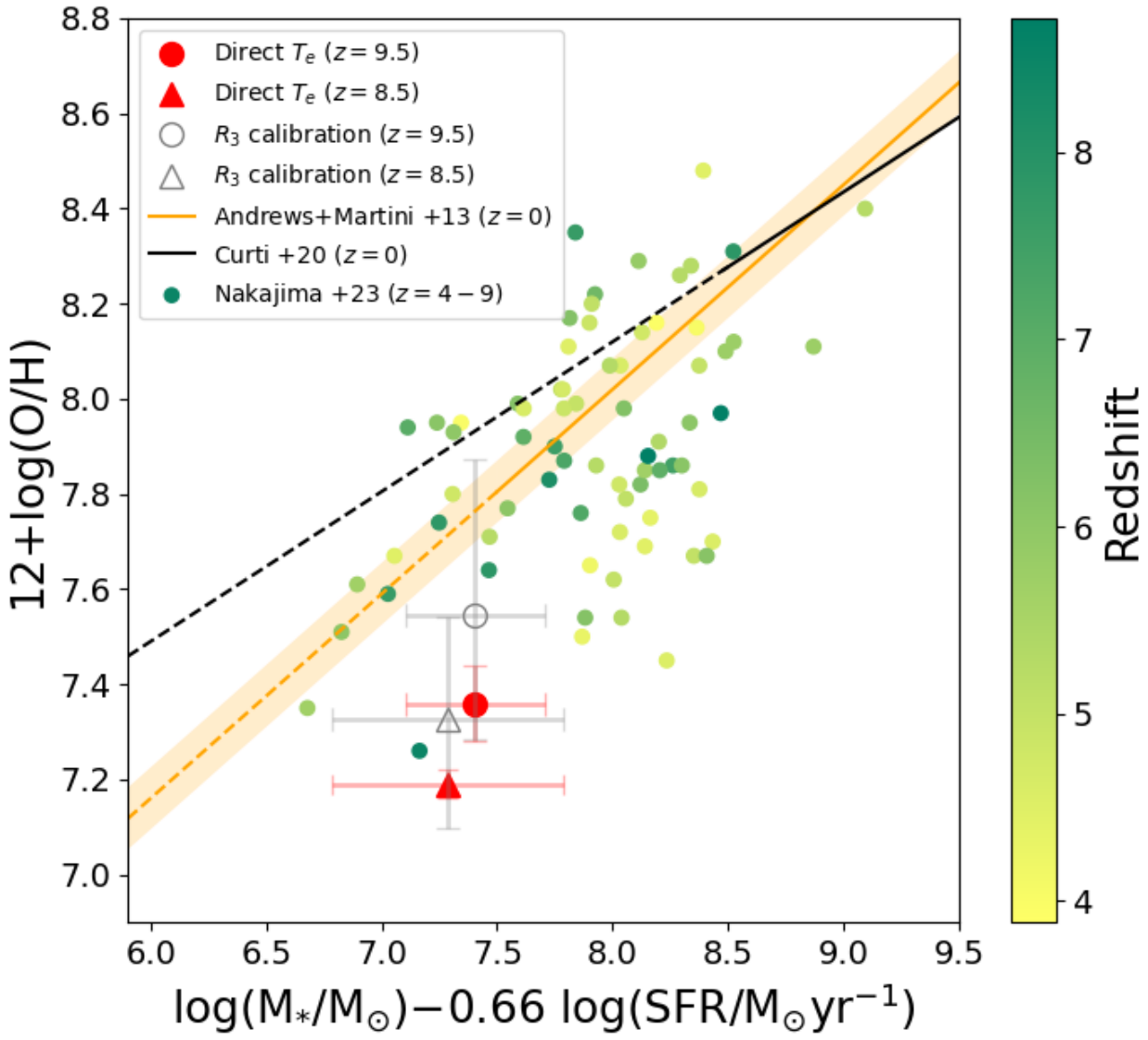

Figure 4.4: The FMR obtained by Andrews and Martini (2013) (orange) and Curti *et al.* (2020) (black) in the local universe $z = 0$, and extrapolated towards lower masses and higher SFRs. The sample of galaxies at redshift $z = 4 - 10$ from Nakajima *et al.* (2023) is plotted, where the points are colored by redshift. Galaxies RXJ_95 and SMACS_85 at $z = 9.5$ and $z = 8.5$ respectively are plotted with errorbars, where the points in red indicate the oxygen abundance obtained using the T_e method, and the points in grey are the oxygen abundance obtained using strong line calibrations.

5 Discussion

In this Chapter I will discuss the findings and results reported in Chapter 4. I will discuss the methods used to obtain the oxygen abundances of the two galaxies RXJ_95 and SMACS_85 in Chapter 5.1. In Chapter 5.2, 5.3 and 5.4 I will put the resulting oxygen abundances into a broader context, and discuss them in relation to the empirical scaling relations obtained by different studies presented in Chapter 4.

5.1 Oxygen abundance measurements

I have calculated the oxygen abundance of the galaxies RXJ_95 and SMACS_85 using both the direct T_e method and strong line calibrations, which strengths and weaknesses I will discuss below.

5.1.1 The direct T_e method

Using the direct T_e method, I find oxygen abundances of 7.36 ± 0.08 for RXJ_95 and 7.19 ± 0.02 for SMACS_85. The direct T_e method provides highly precise measurements of the oxygen abundances, with few assumptions about the conditions in the galaxies. It relies on the ionized gas and therefore traces the HII regions of galaxies, where the gas is ionized by hot stars, and where more or less all oxygen atoms are singly or doubly ionized. Also, it is based on the assumption that the gas is in a state of LTE, meaning that the temperature is the same throughout the ionized gas - this is however a reasonable assumption in the HII regions of galaxies.

In Figure 3.7, it can be seen how the electron temperature starts to decrease, and the measure of the oxygen abundance increase, when exceeding a density of $N_e \sim 10^4$ cm^{-3}. At these densities, collisional deexcitation begins to play a role, as described in Chapter 2.2.1. To measure the electron temperature above this density, one would need to obtain a measurement of the density as well. However, in the case of HII regions densities are generally below $N_e < 10^4$ cm^{-3}.

The main issue that has hindered the use of the direct T_e method in some studies, is its practical application that can be challenging in certain instances. Particularly for low-metallicity objects where the oxygen lines are weak and difficult to measure, or for faint high redshift galaxies, where the flux is reduced and excessive noise in the galaxy spectra can be present. Therefore, other methods, such as strong line calibrations, are often necessary to derive the metal abundance, especially for a larger sample of galaxies.

Both RXJ_95 and SMACS_85 are two highly magnified high redshift galaxies, with bright spectra and clear emission lines, including a detection of the auroral line [OIII]$\lambda 4363$, which is needed to apply the direct T_e method. I have a robust measurement of the oxygen abundance of both galaxies through the direct T_e method, which I use to compare to the less robust ones obtained through strong line calibrations.

5.1.2 The strong line calibration method

I have calculated the oxygen abundances using different strong line calibrations obtained by Nakajima *et al.* (2023) for EW(Hβ) $>$ 200Å, see Table 4.1. The reason for this choice of calibration, is explained in Chapter 4.1. I find that the oxygen abundance measurements are consistent with each other when using different strong line ratios for the RXJ_95 galaxy. For the SMACS_85 galaxy, the strong line ratios that depend on the O[II]$\lambda 3727$ line do not give a correct estimate of the oxygen abundance, as this line is not detected in the spectrum, see Figure 3.6 b). This indicates, that as long as the lines are clearly detected in a spectrum, all the line ratios can be utilized to determine the oxygen abundance through the strong line calibrations, however there are still different advantages and disadvantages when making the choice of line ratio, which I have outlined in Chapter 2.2.2.

As the strong line calibrations are empirical calibrations, they have some level of uncertainty and systematic bias. It is important to notice that some of the strong line calibrations can be highly degenerate with other parameters, such as ionization parameter, density and pressure. A variation in these parameters could change the emission line ratios, and thereby mimic or mask changes in the oxygen abundance (Maiolino and Mannucci, 2019). The use of multiple diagnostics, when possible, to check for consistency and minimize the impact of systematic errors, will account for possible errors in the measured oxygen abundance due to potential degeneracies. Additionally, galaxies with high oxygen abundances tend to have stronger emission

lines, making them easier to observe, which can cause the strong line calibrations to be biased towards higher oxygen abundances.

Especially when applied on galaxies that have different physical conditions than the calibration sample, the strong line calibrations should be used carefully. Even though the strong line calibrations from Nakajima *et al.* (2022), and other strong line calibrations available at the moment, have been calibrated using a large sample of galaxies, making them relatively robust and reliable, the calibration samples have been low redshift galaxies with higher stellar masses. It has been implicitly assumed that, as we look further into space, at higher redshifts, these calibrations would hold. However, as conditions in high redshift galaxies may be different from those in nearby galaxies, this could possibly affect the reliability of the calibrations at high redshifts.

For further analysis of empirical scaling relations, I have chosen to use the oxygen abundances obtained from the calibration with the R_3 ratio ($R_3 = [OIII]_{5007}/H_\beta$), which choice is elaborated in Chapter 4.1. Here I find oxygen abundances of 7.5 ± 0.2 and 7.3 ± 0.2 for RXJ_95 and SMACS_85 respectively, which are consistent with the oxygen abundances obtained using the direct T_e method within 1σ. There are however significantly larger uncertainties on the oxygen abundances obtained using the strong line calibrations than those obtained using the direct T_e method. I find that the oxygen abundances obtained through the direct T_e method are smaller than those obtained with the strong line calibrations, which can be attributed to the different uncertainties and factors described above.

The strong line calibration method only requires the measurement of a few strong emission lines in a galaxy spectrum, and as there are many different calibrations depending on different line fluxes, it is almost always possible to use this method when a resolved spectrum is available.

5.2 Comparison to the SFR-M_* main sequence

In Figure 4.2, I have plotted the relationship between the SFR and stellar mass of star forming galaxies, investigated up to redshift $z = 4$ by Speagle *et al.* (2014), and up to redshift $z = 7 - 10$ by Heintz *et al.* (2023a). It is widely known that more massive galaxies have more gas available, as they are bigger, and are thereby able to

form more stars than less massive ones, resulting in an increase in SFR with stellar mass of galaxies. However it should be noted that observations have shown that the sSFR decreases as the mass of the galaxy increases, meaning that lower mass galaxies are forming stars more efficiently relative to their mass compared to higher mass galaxies.

The SFR for a given mass has been shown to increase when the redshift increases (e.g. Speagle *et al.*, 2014, Heintz *et al.*, 2023b). At higher redshifts, the cosmic gas density is higher, providing more fuel for star formation. Also, galaxies at high redshifts are experiencing more turbulence and are more likely to merge with each other, which trigger bursts of star formation, leading to a higher overall SFR at a given stellar mass. RXJ_95 and SMACS_85 are high redshift galaxies, and are expected to have higher SFRs than galaxies in the local universe. In Figure 4.3 it is shown that they evolve approximately as they should according to this, and are in agreement with results from Heintz *et al.* (2023b) of redshifts $z = 7 - 10$.

It is notable that between the SFR-M_* main sequence relations there is a smaller span from redshift $z = 2$ to $z = 4$ than from $z = 0$ to $z = 2$, and an even smaller span to $z = 7 - 10$. This is due to the fact that redshift does not evolve linearly with look-back time, and as the universe expands, the rate of expansion increases due to the influence of dark energy. This means that the time between different redshift values increases as the redshift gets lower. The fact that the SFR-M_* main sequence relation seems to lie closer and closer together with increasing redshift indicates that the SFR per mass has followed a somewhat steady linear decrease as the universe has aged.

5.3 Comparison to the MZR

In Figure 4.3, I have plotted MZRs obtained by different studies (Curti *et al.*, 2020, Curti *et al.*, 2017, Sanders *et al.*, 2021, Heintz *et al.*, 2023b) at various redshifts. There is a consensus on the MZR in the local universe, where Curti *et al.* (2020), Andrews and Martini (2013), and Sanders *et al.* (2021) find very similar relations. Common for all obtained MZRs is that, as the stellar mass increases, the metallicity tends to increase as well. More massive galaxies typically have a higher number of stars, and therefore more opportunities to produce heavy elements, as these are created in the stars. Additionally, more massive galaxies have stronger gravitational potentials, which can lead to greater retention and recycling of the metals.

It is also shown in Figure 4.3 that as the redshift increases, the oxygen abundance for a given mass decreases. This is in agreement with the observations of the RXJ_95 and SMACS_85 galaxies, which align with the MZR obtained by Heintz *et al.* (2023b) at redshift $z = 7 - 10$. Metals are ejected into the ISM via supernovae explosions and stellar winds. As more and more stars form and evolve over time, the abundance of metals in the ISM increases. The observed decrease in oxygen abundance for a given stellar mass with increasing redshift can thereby be explained by the fact that galaxies at higher redshift are younger and have had less time to build up metals.

The MZRs plotted in Figure 4.3 do not seem to evolve with redshift in the same way as the SFR-M_* main sequence relations discussed in Chapter 5.2. In Figure 4.2, the span between the SFR-M_* main sequence relations decrease with increasing redshift, while in Figure 4.3 the same decrease of the MZRs with increasing redshift is not observed. Again, as the redshift does not evolve linearly with look-back time, this indicates that the oxygen abundance per mass had a steeper increase in the early universe, which became more and more flattened as time passed.

5.4 Comparison to the FMR

The metal abundance has been observed to correlate with different galactic properties, one of which is an anti-correlation between the metal abundance and SFR, at a fixed stellar mass, observed and characterized through the FMR.

5.4.1 The interpretation of the FMR

The FMR arises from the complex interplay among gas inflow, outflow, and star formation in galaxies. Due to these processes, baryons, which are the building blocks of matter, undergo cycling through different phases as a galaxy evolves. Figure 5.1 illustrates how baryons are cycled on a large scale in galaxies.

Metal poor gas gets accreted onto galaxies from the IGM. This gas is primarily composed of hydrogen, with very small amounts of heavier elements. As the gas cools and condenses, it forms dense clouds in the ISM, where it can undergo gravitational collapse and form stars. As stars evolve, they produce metals via nucleosynthesis, and through supernova explosions and stellar winds the ISM gradually gets chemically

enriched by these metals. The newly formed massive stars inject energy and momentum into the gas, driving large-scale outflows that transport gas and metals out of the galaxy. The ejected enriched gas can either escape the gravitational potential well of the galaxy to enrich the IGM or reaccrete onto the galaxy and enrich the inflowing gas.

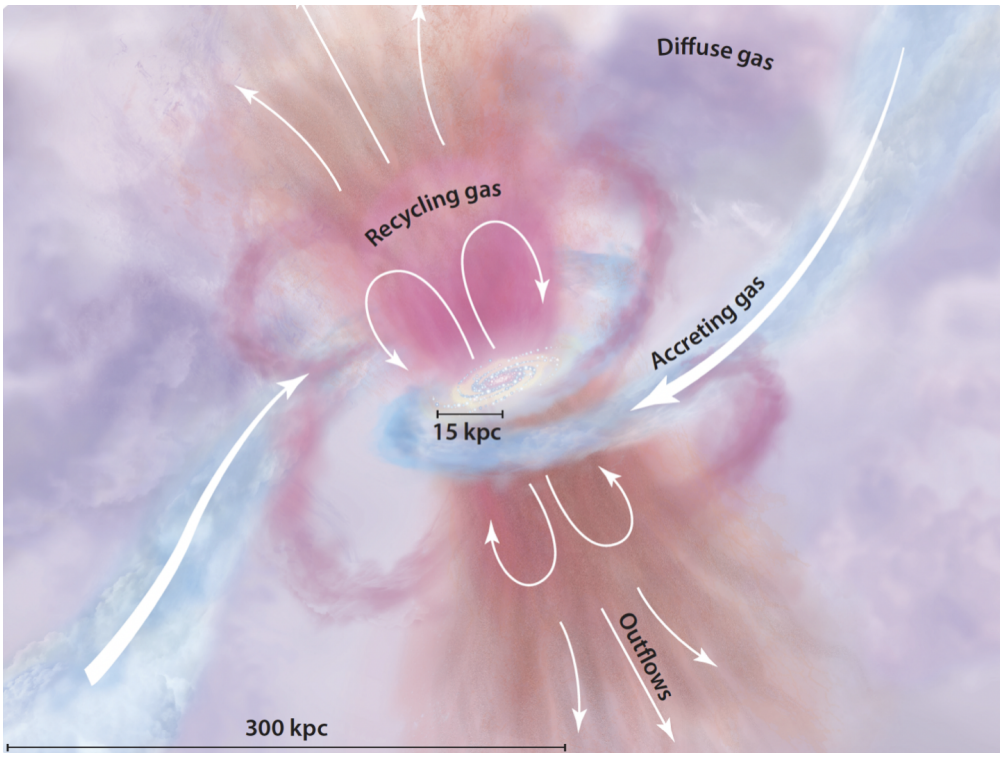

Figure 5.1: Illustration of how baryons are cycled in a galaxy (Tumlinson *et al.*, 2017).

Inflows and outflows in a galaxy are highly dependent on its mass. High mass galaxies have larger gravitational potentials, causing them to hold onto larger amounts of gas, thereby preventing the same amount of galactic outflows as for low-mass galaxies, and are additionally capable of attracting larger amounts of gas from their surroundings (Chisholm *et al.*, 2018). While the large inflows of metal poor gas may temporarily dilute the metal abundance of the galaxy, they provide the raw materials for star formation over longer periods, ultimately leading to an enrichment of metals. The cycling of baryons in and out of galaxies directly impacts the stellar mass, SFR and oxygen abundance of the galaxies. Thus, the correlation between these parameters and their evolution, serve as crucial observational constraints for galaxy evolution models that attempt to understand the build up of galaxies across cosmic time.

At high redshifts, galaxies are generally less massive as they are observed in an earlier stage of their evolution and have had less time to accrete mass and evolve stars. The environment in the early universe around galaxies was more dense and compact than today, and as a result, the SFR per mass was higher in the early universe. In the local

universe however, the galaxies have had time to grow and become more massive, and the SFR per mass has decreased over time as the gas within galaxies has been gradually depleted. Even though galaxies at different redshifts may have different properties, it has been suggested that galaxies evolve through a smooth baryonic growth process in a state of near-equilibrium, which would cause them to follow the same underlying relationship between metal abundance, SFR, and stellar mass that is described by the FMR. Galaxies at different redshifts are expected to sample different parts of the FMR as they evolve and change over cosmic time. The fact that galaxies are more massive and less star-forming in the local universe causes the galaxy samples, and thereby the model range of the FMRs, to shift towards higher $log(M_*) - \alpha * log(SFR)$ values. While the galaxies in the high redshift universe, generally have lower masses and higher SFRs, which causes them to shift towards lower $log(M_*) - \alpha * log(SFR)$ values.

The FMR has mostly been investigated in the local universe, where there is a broad agreement on how the galactic properties depend on each other. In Figure 4.4 I have plotted the FMRs obtained by Andrews and Martini (2013) and Curti *et al.* (2020) at redshift $z \sim 0$, which seems to agree well with each other within their calibration range. The two galaxies RXJ_95 and SMACS_85 do not overlap with the calibration range from the models in the local universe, as they have lower masses. To use the relations obtained by Andrews and Martini (2013) and Curti *et al.* (2020) on high redshift galaxies, I have extrapolated them linearly towards lower $log(M_*) - \alpha * log(SFR)$ values. Whether this is reasonable, and whether a linear or a more complex relation should be used, is something that can be investigated in detail once more JWST data becomes available and a larger spectroscopic sample of high redshift galaxies and their metal abundances is obtained.

5.4.2 Previous findings

The FMR was first introduced by Mannucci *et al.* (2010), that found that the scatter in the oxygen abundance in the MZR could be reduced by accounting for the SFR. It has since then been investigated in many different observational studies (Mannucci *et al.*, 2010, Curti *et al.*, 2020, Andrews and Martini, 2013, Kashino *et al.*, 2016, Troncoso *et al.*, 2014, Heintz *et al.*, 2023b, Baker *et al.*, 2022), and at different redshifts, where there is found evidence that the FMR holds up to at least redshift $z \sim 3$ (Henry *et al.*, 2021, Cresci *et al.*, 2019, Sanders *et al.*, 2021, Lara-Lopez *et al.*, 2010, Maier *et al.*, 2014, Mannucci *et al.*, 2010). Some studies find that galaxies at redshifts $z \sim 2 - 3$ show larger dispersion than local galaxies. However, it is unclear whether this is caused by

intrinsic dispersion related to different evolutionary stages of the galaxies or by larger uncertainties in the estimates of metal abundance, stellar mass, and SFR (Mannucci *et al.*, 2010). The overall picture so far is that the FMR is a robust empirical relation that holds across a range of galaxy types and redshifts. At even higher redshifts $z > 3$, there has been debate about whether there is an anti-correlation or whether galaxies follow the FMR. However, due to the limited spectroscopic data at these redshifts before the JWST, it has previously not been possible to study the FMR in the very high redshift universe.

With the newly acquired data from the JWST, it is now possible to empirically study the FMR at redshifts $z > 7$, and smaller samples have already been gathered and analyzed (Heintz *et al.*, 2023b, Nakajima *et al.*, 2023, Curti *et al.*, 2023). The results from Nakajima *et al.* (2023) are also plotted in Figure 4.4. They do not find any evolution in the FMR up to redshift $z \sim 8$, but a significant decrease in the data points from the local FMR at redshifts $z > 8$. Heintz *et al.* (2023b) finds that there seems to be an offset towards lower metallicities at redshift $z > 7$, which is in agreement with Curti *et al.* (2023), that finds a deviation at redshifts $z > 6$. An offset from the FMR, is also what I find for the RXJ_95 and SMACS_85 galaxies, see Figure 4.4.

5.4.3 A deviation from the FMR at high redshifts

I find that RXJ_95 and SMACS_85 deviates from the FMRs obtained by Andrews and Martini (2013) and Curti *et al.* (2020), shown in Figure 4.4. I find especially a large deviation when the oxygen abundance is obtained from the direct T_e method, which is generally considered a more robust method than the strong line calibration method. For RXJ_95, the oxygen abundance obtained using the T_e method lie $\sim 4\sigma$ below the FMR obtained by Andrews and Martini (2013), while it for the SMACS_85, lie more than 10σ below.

This deviation suggests that galaxies has a lower gas phase oxygen abundance in the early universe, than predicted by the FMR. This might reveal prominent accretion of pristine gas down to at least redshift $z \sim 8 - 9$, happening on timescales shorter than the gas depletion, star-formation, ISM enrichment and mixing compared to lower redshift galaxies (Curti *et al.*, 2023). At this time, the gas that is getting accreted will be mainly hydrogen and have extremely low metal abundance. If the galaxies at redshift $z \sim 8 - 9$ are experiencing large gas accretion, it will cause a dilution of the chemical abundances in the ISM, and a decrease in the metal abundance, as this is measured

with respect to hydrogen, see Equation 2.3. The deviation from the FMR could in principle also be explained by metals being more efficiently removed from the ISM by supernovae driven outflows at high redshifts. Further investigation into this possibility could involve studying the morphology of galaxies in relation to their position on the FMR (Tacchella *et al.*, 2023).

It is also important to mention the possibility that the two galaxies RXJ_95 and SMACS_85 just are having very extreme conditions. If either their masses were smaller or their SFRs higher, this would cause the two data points to be shifted towards lower $log(M_*) - \alpha * log(SFR)$ values and align with the extrapolated FMR for the local universe. However, I find it unlikely that the deviation of the RXJ_95 and SMACS_85 galaxies from the FMR in Figure 4.4 is due to their SFR or stellar mass. This is because the relative SFRs and stellar masses of these galaxies appear to be in line with expectations for the evolution of high redshift galaxies, as illustrated in Figure 4.2. I therefore find it more likely that the deviation from the FMR is due to a greater decrease in the metal abundance at these high redshifts than previously expected, which is also suggested by Heintz *et al.* (2023b).

When comparing the metal abundances, SFRs, and stellar mass measurements, as well as FMR predictions obtained by different studies, there will always be offsets due to different galaxy samples that have been used and assumptions that have been adopted. The stellar masses, SFRs and metal abundances have not all been obtained in a consistent way for the various studies I have compared my results to, which may be contributing to offsets between them. However, assuming that the FMR for the local universe can be extrapolated towards lower masses and higher SFR, there seems to be a significant offset between the FMR and the oxygen abundance measurements obtained with the direct T_e method, even when taking into account the systematic uncertainties that occurs when different studies are compared.

5.4.4 Future outlook

In this study, I have examined the two high redshift galaxies RXJ_95 and SMACS_85. To confidently validate their behavior and eliminate the possibility of them being potential outliers, a more statistically representative sample of early galaxy observations with JWST would be necessary.

JWST has already begun to revolutionise our view of the high redshift Universe, opening a new window onto early galaxy formation and evolution. With NIRSpec, spectroscopic observations of galaxies within the first few Myr after Big Bang, have become possible. In this context the study of the gas phase oxygen abundance via rest-frame optical spectroscopy up to redshifts $z \sim 10$ (Curti *et al.*, 2023) can now be obtained.

As mentioned, recent studies have already investigated the chemical abundances of high redshift galaxies using data obtained with JWST (Heintz *et al.*, 2023b, Nakajima *et al.*, 2023, Curti *et al.*, 2023). The majority of these studies are based on metal abundance determinations from strong emission line ratios that have been calibrated on local samples of galaxies. As the rate of auroral line detections at high redshifts is now rapidly increasing thanks to the JWST, it will be possible to estimate the metal abundance on a large number of galaxies using the robust direct T_e method. This will also allow for re-calibration of the classical strong line diagnostics in the high redshift Universe, which has already been aimed by Sanders *et al.* (2023). As JWST continue to gather data, the robustness of the samples of early galaxies are continuously improving. This is crucial for future studies to provide a tighter constraint on the FMR at high redshifts and a more comprehensive picture on the processes regulating early galaxy formation and evolution across cosmic time.

Conclusion

6

In this thesis, I have explored the chemical enrichment of galaxies within 600 Myr after the Big Bang, at redshifts $z \sim 8-10$. By investigating the interplay between the chemical abundances of galaxies and other galactic properties at various cosmic times, I have gained insight into the underlying physics driving the chemical enrichment of galaxies at high redshifts.

As an introduction to the topic of spectroscopy, I analyzed spectroscopic data obtained with MOSFIRE. This analyze involved examining $\sim$ 1000 two-dimensional spectra of observations that coincided with those from the JWST CEERS program. I collected the wavelengths of every visible emission line, both from the central galaxies intended for observation and from serendipitous galaxy detections that were present in some of the observations. I gathered detections of the same galaxies taken in different bands, and converted the two-dimensional spectra into $\sim$ 300 unique one-dimensional spectra. Furthermore, I created a catalog of information for each galaxy observation.

I then turned my attention to analyzing spectroscopic data obtained with NIRSpec on JWST. Specifically, I focused on studying two low mass galaxies with high redshifts: RXJ_95 and SMACS_85. I find that RXJ_95 has a spectroscopic redshift of $z = 9.5013 \pm 10^{-4}$. It is highly magnified by the foreground galaxy cluster RXJ2129, with a magnification factor of $\mu = 19.2 \pm 3.6$. Meanwhile, SMACS_85 has a spectroscopic redshift of $z = 8.4956 \pm 10^{-4}$ and is magnified by the galaxy cluster MACS J0723.3-7327, with a magnification factor of $\mu = 8.69 \pm 2.61$.

I analyzed the two galaxy spectra using a continuum model with Gaussian line profiles to estimate the spectroscopic redshift and line fluxes, including error estimations. I then calculated several parameters such as line flux ratios, UVβ slopes, equivalent widths, and SFRs. The auroral emission line [OIII]λ4363 is present in both galaxy spectra, which allowed me to measure the oxygen abundance via the direct T_e method. This approach relies on the sensitivity of the [OIII]λ4363/([OIII]λ4959+λ5007) ratio to the electron temperature in ionized gas, which can be used to determine the oxygen abundance. Using the direct T_e method, I measured the oxygen abundance for RXJ_95

to be 7.36 ± 0.08 and for SMACS_85 to be 7.19 ± 0.02. For comparison reasons, I also estimated the oxygen abundance using strong line calibrations, that relate the oxygen abundance to strong emission line ratios. I used the calibration from Nakajima *et al.* (2022) for H$\beta(EW) > 200$ Å and the R_3 =[OIII]5007/Hβ ratio to obtain an oxygen abundance of 7.5 ± 0.2 for RXJ_95 and 7.3 ± 0.2 for SMACS_85. However, as the auroral line [OIII]λ4363 is detected in both galaxy spectra, I consider the oxygen abundances measured from the direct T_e method more reliable than the ones obtained from strong line calibrations.

To gain a perspective on the measured oxygen abundances, I investigated empirical scaling relations between galactic properties obtained by other studies, both in the local and the high redshift universe. Comparing RXJ_95 and SMACS_85 to the SFR-M_* main sequence, they are found to lie above the relation obtained in the local universe, indicating a higher SFR given their stellar mass, which is as expected at higher redshifts. Additionally, when comparing the galaxies to the local MZR, they have lower oxygen abundance given their stellar mass than galaxies in the local universe, which is also as expected at higher redshifts.

There appears to be a deviation when comparing the SFRs, stellar masses, and oxygen abundances of RXJ_95 and SMACS_85 to the FMR, which is a universal relation meant to describe the equilibrium between these properties. The deviation suggests that there could be a lower oxygen abundance in galaxies in the early universe than predicted by the FMR. This implies that galaxies down to at least $z \sim 8 - 9$ may still be closely connected with the IGM and subject to continuous infall of metal poor gas which effectively dilutes their metal abundances.

The JWST has provided high-quality spectroscopic data that enables more detailed observations in the high redshift universe ($z > 7$) than ever before. With more spectroscopic observations of high redshift galaxies in the future, it will be possible to further constrain the FMR in the very early universe. This will be a powerful tool for gaining a deeper understanding of the properties of early galaxies and the processes driving their evolution over cosmic time.

7 Bibliography

Andrews, B. H. and P. Martini (Mar. 2013). „The Mass-Metallicity Relation with the Direct Method on Stacked Spectra of SDSS Galaxies“. In: *The Astrophysical Journal* 765.2, 140, p. 140. arXiv: 1211.3418 [astro-ph.CO].

Asplund, M., N. Grevesse, A. J. Sauval, and P. Scott (Sept. 2009). „The Chemical Composition of the Sun“. In: *Annual Review of Astronomy and Astrophysics* 47.1, pp. 481–522. arXiv: 0909.0948 [astro-ph.SR].

Baker, W. M., R. Maiolino, F. Belfiore, M. Curti, A. F. L. Bluck, L. Lin, S. L. Ellison, M. Thorp, and H. Pan (Dec. 2022). „The metallicity's fundamental dependence on both local and global galactic quantities“. In: *Monthly Notices of the Royal Astronomical Society* 519.1, pp. 1149–1170. arXiv: 2210.03755 [astro-ph.GA].

Bhatawdekar, R. and C. J. Conselice (Mar. 2021). „UV Spectral Slopes at z = 6-9 in the Hubble Frontier Fields: Lack of Evidence for Unusual or Population III Stellar Populations“. In: *The Astrophysical Journal* 909.2, p. 144. arXiv: 2006.00013 [astro-ph.GA].

Bian, F., L. Kewley, and M. Dopita (June 2018). „“Direct” Gas-phase Metallicity in Local Analogs of High-redshift Galaxies: Empirical Metallicity Calibrations for High-redshift Star-forming Galaxies“. In: *The Astrophysical Journal* 859, p. 175. arXiv: 1805.08224 [astro-ph.GA].

Birkmann, S. M., P. Ferruit, G. Giardino, *et al.* (May 2022). „The Near-Infrared Spectrograph (NIRSpec) on the James Webb Space Telescope“. In: *Astronomy & Astrophysics* 661, A83. arXiv: 2202.03309 [astro-ph.IM].

Brammer, G. (May 2019). *Grizli: Grism redshift and line analysis software*. Astrophysics Source Code Library, record ascl:1905.001. ascl: 1905.001. URL: https://ui.adsabs.harvard.edu/abs/2019ascl.soft05001B.

Brammer, G. (May 2022a). *MOFFIRE database*. URL: https://s3.amazonaws.com/grizli-v2/DatabaseSchema/index.html.

Brammer, G. (Nov. 2022b). *msaexp: NIRSpec analyis tools*. Version 0.3. URL: https://github.com/gbrammer/msaexp.

Brammer, G. *CEERS and MOSFIRE observations*. Accessed: 2023-05-18. URL: https://s3.amazonaws.com/grizli-v2/ClusterTiles/Map/egs/index.html?ra=214.9317634&dec=52.9104287&zoom=4.

Calzetti, D., A. L. Kinney, and T. Storchi-Bergmann (July 1994). „Dust Extinction of the Stellar Continua in Starburst Galaxies: The Ultraviolet and Optical Extinction Law“. In: *The Astrophysical Journal* 429, p. 582. URL: https://ui.adsabs.harvard.edu/abs/1994ApJ...429..582C.

Carnall, A C, R J McLure, J S Dunlop, and R Davé (Aug. 2018). „Inferring the star formation histories of massive quiescent galaxies with bagpipes: evidence for multiple quenching mechanisms“. In: *Monthly Notices of the Royal Astronomical Society* 480.4, pp. 4379–4401. arXiv: 1712.04452 [astro-ph.GA].

Chisholm, J., C. Tremonti, and C. Leitherer (Sept. 2018). „Metal-enriched galactic outflows shape the mass–metallicity relationship“. In: *Monthly Notices of the Royal Astronomical Society* 481.2, pp. 1690–1706. arXiv: 1808.10453 [astro-ph.GA].

Cresci, G., F. Mannucci, and M. Curti (June 2019). „Fundamental metallicity relation in CALIFA, SDSS-IV MaNGA, and high-iz/i galaxies“. In: *Astronomy & Astrophysics* 627, A42. arXiv: 1811.06015 [astro-ph.GA].

Curti, M., G. Cresci, F. Mannucci, A. Marconi, R. Maiolino, and S. Esposito (Feb. 2017). „New fully empirical calibrations of strong-line metallicity indicators in star-forming galaxies“. In: *Monthly Notices of the Royal Astronomical Society* 465.2, pp. 1384–1400. arXiv: 1610.06939 [astro-ph.GA].

Curti, M., R. Maiolino, S. Carniani, *et al.* (2023). „JADES: Insights on the low-mass end of the mass–metallicity–star-formation rate relation at $3 < z < 10$ from deep JWST/NIRSpec spectroscopy“. In: *arXiv e-prints*. arXiv: 2304.08516 [astro-ph.GA].

Curti, M., F. Mannucci, G. Cresci, and R. Maiolino (Jan. 2020). „The mass-metallicity and the fundamental metallicity relation revisited on a fully T_e-based abundance

scale for galaxies“. In: *Monthly Notices of the Royal Astronomical Society* 491.1, pp. 944–964. arXiv: 1910.00597 [astro-ph.GA].

Dunlop, J. S., A. B. Rogers, R. J. McLure, *et al.* (July 2013). „The UV continua and inferred stellar populations of galaxies at z 7-9 revealed by the Hubble Ultra-Deep Field 2012 campaign“. In: *Monthly Notices of the Royal Astronomical Society* 432.4, pp. 3520–3533. arXiv: 1212.0860 [astro-ph.CO].

Ellison, S. L., L. Simard, N. B. Cowan, I. K. Baldry, D. R. Patton, and A. W. McConnachie (July 2009). „The mass-metallicity relation in galaxy clusters: the relative importance of cluster membership versus local environment“. In: *Monthly Notices of the Royal Astronomical Society* 396.3, pp. 1257–1272. arXiv: 0903.4684 [astro-ph.CO].

Fan, X., M. A. Strauss, R. H. Becker, R. L. White, J. E. Gunn, G. R. Knapp, G. T. Richards, D. P. Schneider, J. Brinkmann, and M. Fukugita (July 2006). „Constraining the Evolution of the Ionizing Background and the Epoch of Reionization with z$\sim$6 Quasars. II. A Sample of 19 Quasars“. In: *The Astronomical Journal* 132.1, pp. 117–136. arXiv: astro-ph/0512082 [astro-ph].

Giménez-Arteaga, C., P. A. Oesch, G. Brammer, *et al.* (2022). „Spatially Resolved Properties of High Redshift Galaxies in the SMACS0723 JWST ERO Field“. In: *arXiv e-prints*. arXiv: 2212.08670 [astro-ph.GA].

Harikane, Y., M. Ouchi, M. Oguri, Y. Ono, K. Nakajima, Y. Isobe, H. Umeda, K. Mawatari, and Y. Zhang (Feb. 2023). „A Comprehensive Study of Galaxies at z $\sim$ 9–16 Found in the Early JWST Data: Ultraviolet Luminosity Functions and Cosmic Star Formation History at the Pre-reionization Epoch“. In: *The Astrophysical Journal Supplement Series* 265.1, p. 5. arXiv: 2208.01612 [astro-ph.GA].

Heintz, K. E., Gabriel B. Brammer, Clara Giménez-Arteaga, *et al.* (2023b). „Dilution of chemical enrichment in galaxies 600 Myr after the Big Bang“. In: *arXiv e-prints*. arXiv: 2212.02890 [astro-ph.GA].

Heintz, K. E., C. Giménez-Arteaga, S. Fujimoto, *et al.* (Feb. 2023a). „The Gas and Stellar Content of a Metal-poor Galaxy at z = 8.496 as Revealed by JWST and ALMA“. In: *The Astrophysical Journal Letters* 944.2, p. L30. arXiv: 2212.06877 [astro-ph.GA].

Henry, A., M. Rafelski, B. Sunnquist, *et al.* (Oct. 2021). „The Mass–Metallicity Relation at z $\sim$ 1–2 and Its Dependence on the Star Formation Rate“. In: *The Astrophysical Journal* 919.2, p. 143. arXiv: 2107.00672 [astro-ph.GA].

Huang, R., A. J. Battisti, K. Grasha, E. da Cunha, C. P. Lagos, S. K. Leslie, and E. Wisnioski (Mar. 2023). „Exploring the intrinsic scatter of the star-forming galaxy main sequence at redshift 0.5 to 3.0“. In: 520.1, pp. 446–460. arXiv: 2301.01995 [astro-ph.GA].

Izotov, Y. I., G. Stasinska, G. Meynet, N. G. Guseva, and T. X. Thuan (Mar. 2006). „The chemical composition of metal-poor emission-line galaxies in the Data Release 3 of the Sloan Digital Sky Survey“. In: *Astronomy &amp Astrophysics* 448.3, pp. 955–970. arXiv: astro-ph/0511644 [astro-ph].

JWST User Documentation (JDox) (Jan. 2016). JWST User Documentation Website. URL: https://jwst-docs.stsci.edu/jwst-near-infrared-spectrograph/nirspec-instrumentation/nirspec-dispersers-and-filters.

Kalirai, J (July 2018). „Scientific discovery with the James Webb Space Telescope“. In: *Contemporary Physics* 59.3, pp. 251–290. arXiv: 1805.06941 [astro-ph.IM].

Kashino, D., A. Renzini, J. D. Silverman, and E. Daddi (May 2016). „Hide-and-seek with the Fundamental Metallicity Relation“. In: *The Astrophysical Journal* 823.2, p. L24. arXiv: 1605.03586 [astro-ph.GA].

Kennicutt, R. C. (Sept. 1998). „Star Formation in Galaxies Along the Hubble Sequence“. In: *Annual Review of Astronomy and Astrophysics* 36.1, pp. 189–231. arXiv: astro-ph/9807187 [astro-ph].

Kroupa, P. (Apr. 2001). „On the variation of the initial mass function“. In: *Monthly Notices of the Royal Astronomical Society* 322.2, pp. 231–246. arXiv: astro-ph/0009005 [astro-ph].

Lara-Lopez, M. A., J. Cepa, A. Bongiovanni, A. M. Perez Garcia, A. Ederoclite, H. Castaneda, M. Fernandez Lorenzo, M. Povic, and M. Sanchez-Portal (Oct. 2010). „A fundamental plane for field star-forming galaxies“. In: *Astronomy and Astrophysics* 521, p. L53. arXiv: 1005.0509 [astro-ph.CO].

Liu, A., E. Bulbul, M. E. Ramos-Ceja, *et al.* (Feb. 2023). „X-ray analysis of JWST's first galaxy cluster lens SMACS J0723.3−7327“. In: *Astronomy & Astrophysics* 670, A96. arXiv: 2210.00633 [astro-ph.CO].

Ma, X., P. F. Hopkins, C. Faucher-Giguere, N. Zolman, A. L. Muratov, D. Kerevs, and E. Quataert (Dec. 2015). „The origin and evolution of the galaxy mass–metallicity relation“. In: *Monthly Notices of the Royal Astronomical Society* 456.2, pp. 2140–2156. arXiv: 1504.02097 [astro-ph.GA].

Maier, C., S. J. Lilly, B. L. Ziegler, T. Contini, E. Perez Montero, Y. Peng, and I. Balestra (Sept. 2014). „The Mass-Metallicity and Fundamental Metallicity Relations at z > 2 Using Very Large Telescope and Subaru Near-infrared Spectroscopy of zCOSMOS Galaxies“. In: *The Astrophysical Journal* 792.1, p. 3. arXiv: 1406.6069 [astro-ph.GA].

Maiolino, R. and F. Mannucci (Feb. 2019). „De re metallica: the cosmic chemical evolution of galaxies“. In: *The Astronomy and Astrophysics Review* 27.1, p. 3. arXiv: 1811.09642 [astro-ph.GA].

Maiolino, R., T. Nagao, A. Grazian, *et al.* (Sept. 2008). „AMAZE. I. The evolution of the mass-metallicity relation at z > 3“. In: *Astronomy & Astrophysics* 488.2, pp. 463–479. arXiv: 0806.2410 [astro-ph].

Mancuso, C., A. Lapi, J. Shi, Z. Y. Cai, J. Gonzalez-Nuevo, M. Bethermin, and L. Danese (Dec. 2016). „The Main Sequences of Star-forming Galaxies and Active Galactic Nuclei at High Redshift“. In: *The Astrophysical Journal* 833.2, p. 152. arXiv: 1610.05910 [astro-ph.GA].

Mannucci, F., G. Cresci, R. Maiolino, A. Marconi, and A. Gnerucci (Nov. 2010). „A fundamental relation between mass, star formation rate and metallicity in local and high-redshift galaxies“. In: *Monthly Notices of the Royal Astronomical Society* 408.4, pp. 2115–2127. arXiv: 1005.0006 [astro-ph.CO].

Naidu, R. P., P. A. Oesch, P. van Dokkum, *et al.* (Nov. 2022). „Two Remarkably Luminous Galaxy Candidates at z ≈ 10-12 Revealed by JWST“. In: *The Astrophysical Journal Letters* 940.1, p. L14. arXiv: 2207.09434 [astro-ph.GA].

Nakajima, K., M. Ouchi, Y. Isobe, Y. Harikane, Y. Zhang, Y. Ono, H. Umeda, and M. Oguri (Jan. 2023). „JWST Census for the Mass-Metallicity Star-Formation Relations at

z=4-10 with Self-Consistent Flux Calibration and the Proper Metallicity Calibrators“. In: *arXiv e-prints*. arXiv: 2301.12825 [astro-ph.GA].

Nakajima, K., M. Ouchi, Y. Xu, *et al.* (Sept. 2022). „EMPRESS. V. Metallicity Diagnostics of Galaxies over 12 + log(O/H) 6.9–8.9 Established by a Local Galaxy Census: Preparing for JWST Spectroscopy“. In: *The Astrophysical Journal Supplement Series* 262, p. 3. arXiv: 2206.02824 [astro-ph.GA].

Osterbrock, D. E. and G. J Ferland (2006). *Astrophysics of gaseous nebulae and active galactic nuclei*.

Prevot, M. L., J. Lequeux, E. Maurice, L. Prevot, and B. Rocca-Volmerange (Mar. 1984). „The typical interstellar extinction in the Small Magellanic Cloud.“ In: *Astronomy and Astrophysics* 132, pp. 389–392. URL: https://ui.adsabs.harvard.edu/abs/1984A&A...132..389P.

Rigby, J. (Jan. 2023). „The Science Performance of JWST as Characterized in Commissioning“. In: *Publications of the Astronomical Society of the Pacific* 55, p. 100.01. arXiv: 2207.05632 [astro-ph.IM].

Robertson, Brant E., Richard S. Ellis, James S. Dunlop, Ross J. McLure, and Daniel P. Stark (Nov. 2010). „Early star-forming galaxies and the reionization of the Universe“. In: *Nature* 468.7320, pp. 49–55. arXiv: 1011.0727 [astro-ph.CO].

Robitaille, T. P., E. J. Tollerud, P. Greenfield, *et al.* (Sept. 2013). „Astropy: A community Python package for astronomy“. In: *Astronomy & Astrophysics* 558, A33. arXiv: 1307.6212 [astro-ph.IM].

Sanders, R. L., A. E. Shapley, T. Jones, *et al.* (June 2021). „The MOSDEF Survey: The Evolution of the Mass-Metallicity Relation from z = 0 to z 3.3“. In: *The Astrophysical Journal* 914.1, 19, p. 19. arXiv: 2009.07292 [astro-ph.GA].

Sanders, R. L., A. E. Shapley, M. W. Topping, N. A. Reddy, and G. B. Brammer (Mar. 2023). „Direct T_e-based Metallicities of z=2-9 Galaxies with JWST/NIRSpec: Empirical Metallicity Calibrations Applicable from Reionization to Cosmic Noon“. In: *arXiv e-prints*. arXiv: 2303.08149 [astro-ph.GA].

Sparre, M., C. C. Hayward, V. Springel, M. Vogelsberger, S. Genel, P. Torrey, D. Nelson, D. Sijacki, and L. Hernquist (Jan. 2015). „The star formation main sequence and

stellar mass assembly of galaxies in the Illustris simulation“. In: *Monthly Notices of the Royal Astronomical Society* 447.4, pp. 3548–3563. arXiv: 1409.0009 [astro-ph.GA].

Speagle, J., C. Steinhardt, P. Capak, and J. Silverman (Oct. 2014). „A Highly Consistent Framework for the Evolution of the Star-Forming “Main Sequence” from z $\sim$ 0-6“. In: *The Astrophysical Journal Supplement Series* 214.2, p. 15. arXiv: 1405.2041 [astro-ph.GA].

Table of spectral lines used in SDSS. Accessed: 2023-05-11. URL: https://classic.sdss.org/dr6/algorithms/linestable.html.

Tacchella, S., S. L. Finkelstein, M. Bagley, *et al.* (Mar. 2022). „On the Stellar Populations of Galaxies at z = 9-11: The Growth of Metals and Stellar Mass at Early Times“. In: *The Astrophysical Journal* 927.2, p. 170. arXiv: 2111.05351 [astro-ph.GA].

Tacchella, S., B. D. Johnson, B. E. Robertson, *et al.* (May 2023). „JWST NIRCamNIRSpec: Interstellar medium and stellar populations of young galaxies with rising star formation and evolving gas reservoirs“. In: *Monthly Notices of the Royal Astronomical Society*. arXiv: 2208.03281 [astro-ph.GA].

Troncoso, P., R. Maiolino, V. Sommariva, *et al.* (Mar. 2014). „Metallicity evolution, metallicity gradients, and gas fractions at z $\sim$ 3.4“. In: *Astronomy & Astrophysics* 563, A58. arXiv: 1311.4576 [astro-ph.CO].

Tumlinson, J., M. S. Peeples, and J. K. Werk (Aug. 2017). „The Circumgalactic Medium“. In: *Annual Review of Astronomy and Astrophysics* 55.1, pp. 389–432. arXiv: 1709.09180 [astro-ph.GA].

Valentino, F., G. Brammer, S. Fujimoto, *et al.* (Apr. 2022). „The Archival Discovery of a Strong Ly and [C ii] Emitter at z = 7.677“. In: *The Astrophysical Journal Letters* 929.1, p. L9. arXiv: 2203.03657 [astro-ph.GA].

Wang, F., F. B. Davies, J. Yang, *et al.* (June 2020). „A Significantly Neutral Intergalactic Medium Around the Luminous z = 7 Quasar J0252-0503“. In: *The Astrophysical Journal* 896.1, 23, p. 23. arXiv: 2004.10877 [astro-ph.GA].

Williams, H., P. L. Kelly, W. Chen, *et al.* (Oct. 2022). „A Highly Magnified and Extremely Compact Galaxy at Redshift 9.51 with Strong Nebular Emission“. In: *arXiv e-prints*. arXiv: 2210.15699 [astro-ph.GA].

Wise, J. H. (2023). *The formation of the first black holes*. arXiv: 2304.09311 [astro-ph.HE].

Zaroubi, S. (June 2012). *The Epoch of Reionization*. arXiv: 1206.0267 [astro-ph.CO].

Zitrin, A., A. Fabris, J. Merten, *et al.* (Mar. 2015). „Hubble Space Telescope Combined Strong and Weak Lensing Analysis of the CLASH Sample: Mass and Magnification Models and Systematic Uncertainties“. In: *The Astrophysical Journal* 801.1, p. 44. arXiv: 1411.1414 [astro-ph.CO].

8 Appendix

	target_name	array_agg	nexp	ra	dec	unique_id	offset_pix	wavelengths	offset_arcsec	ra_targ	dec_targ
0	38658	['H']	3	214.77446	52.84820	214.7745_52.8482	66.042151	['None']	0.000000	214.774458	52.848197
1	37375	['H']	3	214.77804	52.84436	214.778_52.8444	30.758442	[17298.081739891986]	0.339417	214.778040	52.844452
2	33376	['H']	3	214.79392	52.84159	214.7939_52.8416	47.206371	['None']	0.000000	214.793917	52.841594
3	25193	['H']	3	214.83087	52.83427	214.8309_52.8343	42.974026	[16133.997664574514]	0.586599	214.830872	52.834438
4	26493	['H']	3	214.81729	52.82982	214.8173_52.8298	52.837142	['None']	0.000000	214.817292	52.829819
...	...	...	...	...	...	...	...	...	...	...	...
1075	33455	['H']	3	214.97750	52.97167	214.9775_52.9717	74.387013	[17153.048314114727]	5.458045	214.977469	52.973188
1076	32761	['H']	6	214.93146	52.93558	214.9315_52.9356	72.485714	[15130.213691431907]	-0.147591	214.931459	52.935534
1077	31542.0	['K']	3	214.84942	52.87312	214.8494_52.8731	84.376623	[21747.225076631148]	3.848433	214.849395	52.874186
1078	EGS_HbO3_424	['J']	3	214.94313	52.91386	214.9431_52.9139	48.158442	[12735.929353379068]	0.693999	214.943121	52.914057
1079	13018120	['J']	3	214.94262	52.91389	214.9426_52.9139	45.069264	[13006.651875638592, 13263.83827178514, 13392....	0.550768	214.942622	52.914045

Figure 8.1: Clipping of MOFFIRE catalogue, that will be released publicly soon.

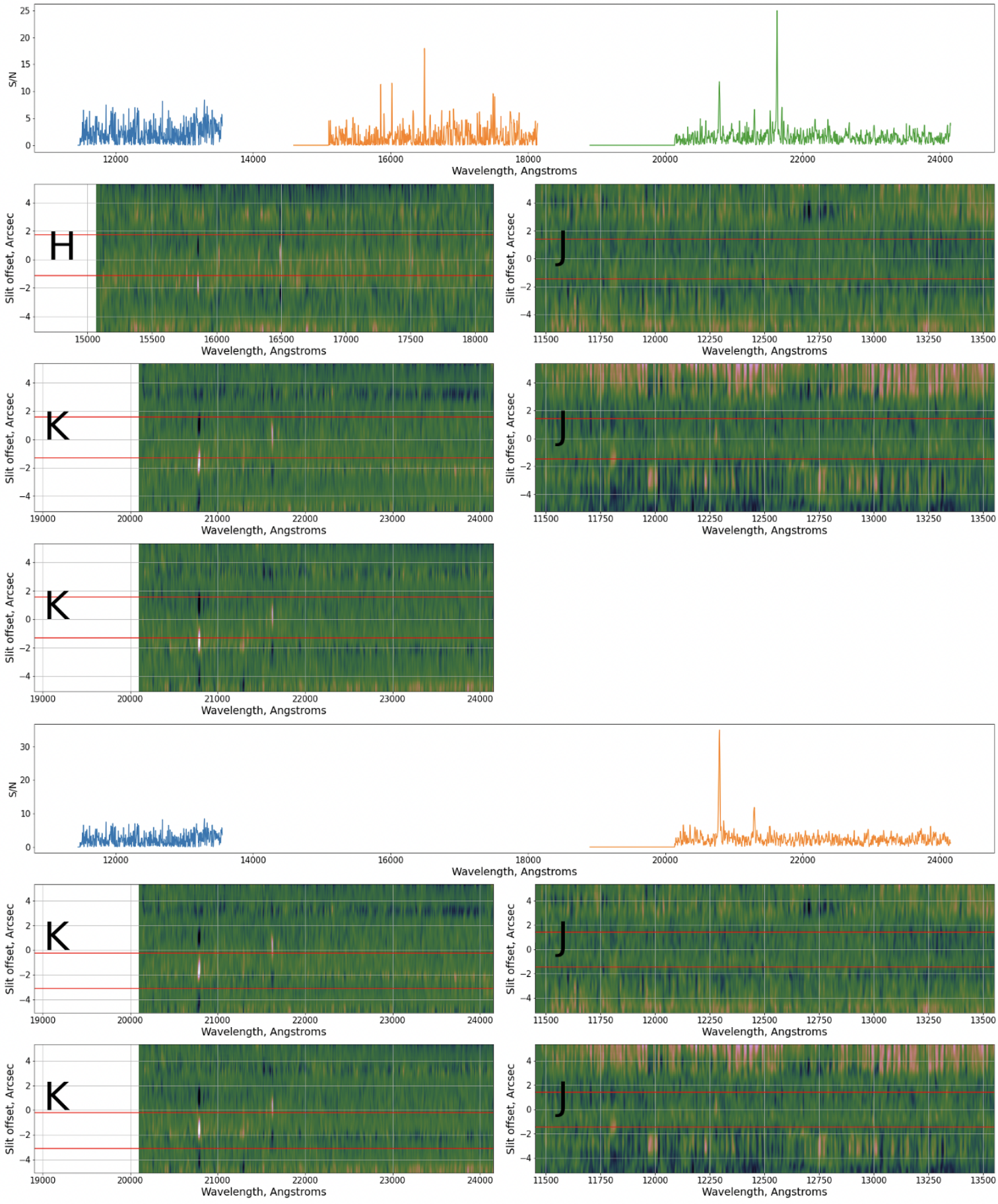

Figure 8.2: Example of a MOSFIRE observation, with a central galaxy, and a serendipitous galaxy detection. In this case two individual one-dimensional spectra has been extracted using different extraction windows (indicated as red horizontal lines).

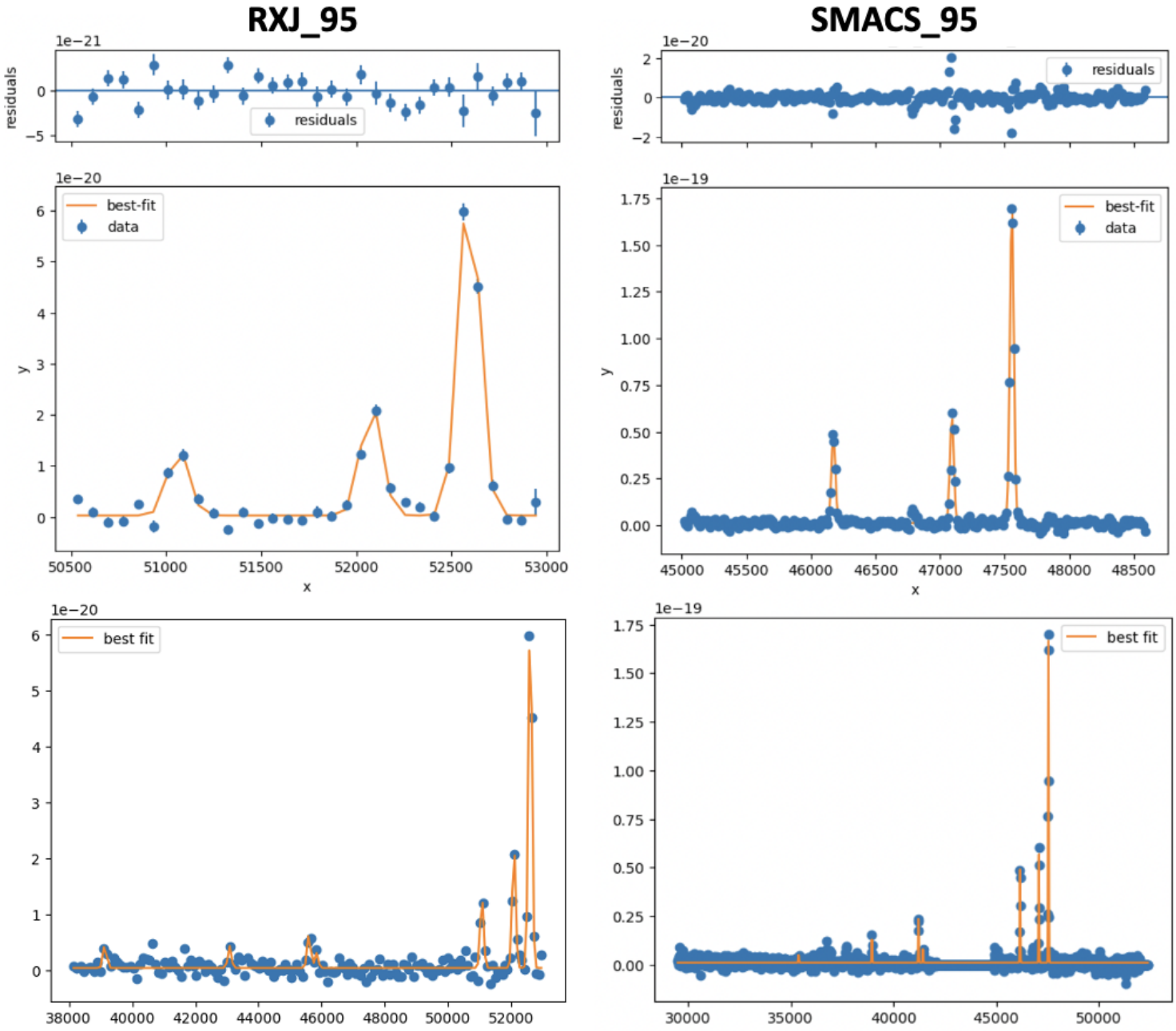

Figure 8.3: Best fit of a continuum model with numerous Gaussian line profiles for the two galaxies RXJ_95 and SMACS_85, using lmfit least squares algorithm with MCMC sampling. The upper figures is a fit of the three strong emission lines $H\beta$, [OIII]λ4960 and [OIII]λ5007 with a corresponding residual plot, while the lower figures are fits of all the emission lines indicated in Figure 3.6.

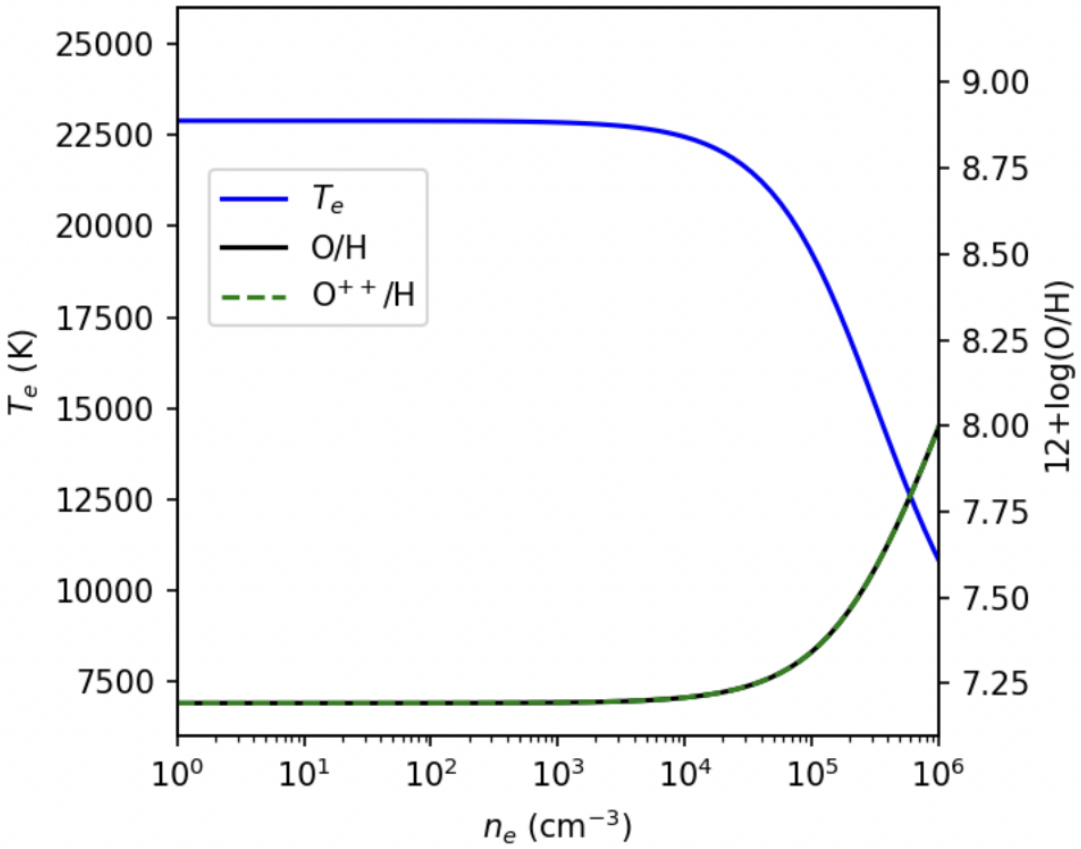

Figure 8.4: Recreated figure from Heintz *et al.* (2023b) of the derived electron temperature T_e and the oxygen abundance $12 + log(O/H)$ for galaxy SMACS_85 as a function of the electron density n_e.

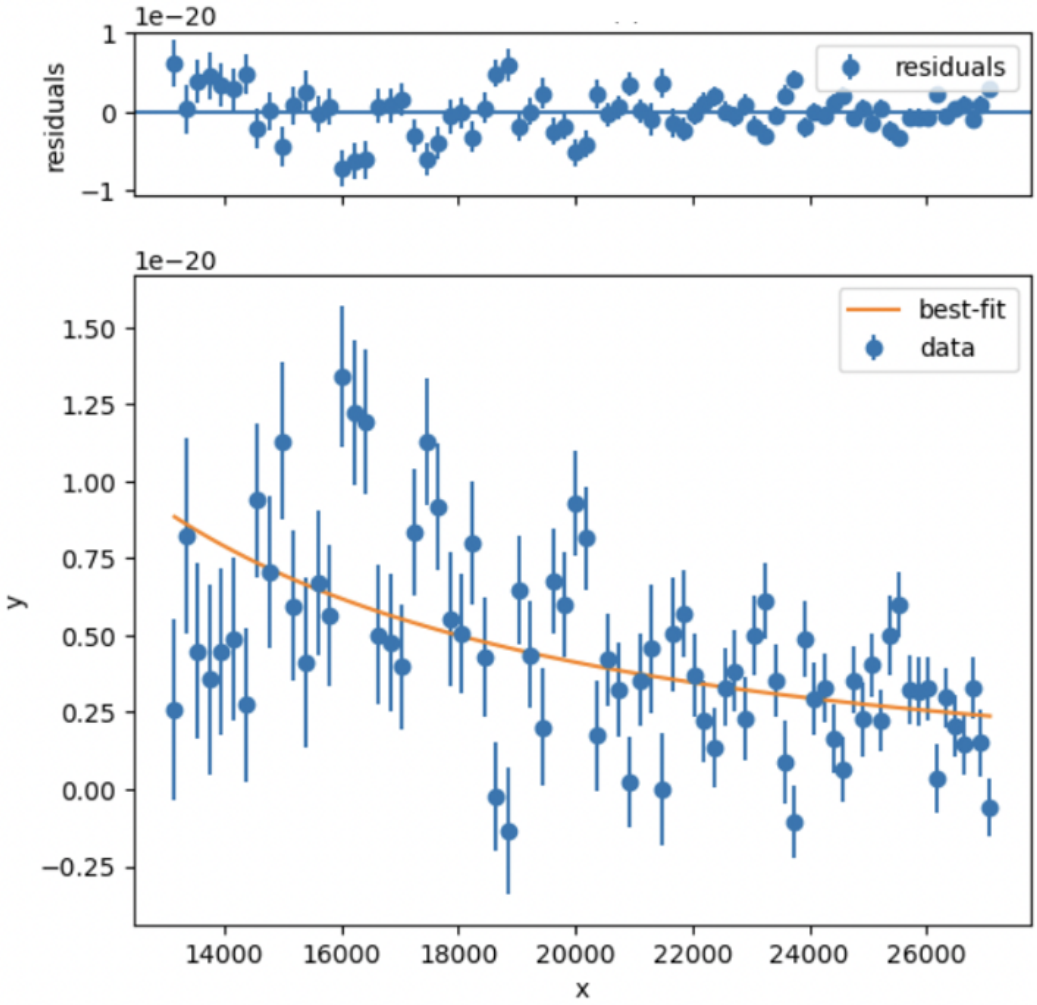

Figure 8.5: Fit of the UVβ slope of the RXJ_95 galaxy using lmfit least squares algorithm with MCMC sampling. The slope is explained further in Chapter 3.2.5.